

1 **Modeling extreme precipitation over East China with a global variable-**  
2 **resolution modeling framework (MPASv5.2): Impacts of resolution and**  
3 **physics**

4 <sup>1</sup>Chun Zhao, <sup>1</sup>Mingyue Xu, <sup>1</sup>Yu Wang\*, <sup>1</sup>Meixin Zhang, <sup>2</sup>Jianping Guo, <sup>3</sup>Zhiyuan Hu, <sup>4</sup>L.  
5 Ruby Leung, <sup>5</sup>Michael Duda, <sup>5</sup>William Skamarock

6  
7  
8 <sup>1</sup>School of Earth and Space Sciences, University of Science and Technology of China, Hefei,  
9 China

10 <sup>2</sup>State Key Laboratory of Severe Weather, Chinese Academy of Meteorological Sciences,  
11 Beijing, China

12 <sup>3</sup>Key Laboratory for Semi-Arid Climate Change of the Ministry of Education, Lanzhou  
13 University, Gansu, China

14 <sup>4</sup>Atmospheric Sciences and Global Change Division, Pacific Northwest National Laboratory,  
15 Richland, WA, USA

16 <sup>5</sup>National Center for Atmospheric Research, Boulder, CO, USA

17  
18  
19 Manuscript for submission to Geoscientific Model Development

20  
21  
22 \*Corresponding authors: Yu Wang (wangyu09@ustc.edu.cn)

23  
24 **Key points:**

- 25 1. MPAS simulations at global uniform and variable resolutions share similar characteristics  
26 of precipitation and wind in the refined region.  
27 2. Numerical experiments reveal significant impacts of resolution on simulating the distribution  
28 and intensity of precipitation and updrafts.  
29 3. Study provides evidence supporting the use of convection-permitting global variable-  
30 resolution simulation for studying extreme precipitation.

32 **Abstract**

33           The non-hydrostatic atmospheric Model for Prediction Across Scales (MPAS-A), a  
34 global variable-resolution modeling framework, is applied at a range of resolutions from  
35 hydrostatic (60 km, 30 km, 16 km) to non-hydrostatic (4 km) scales using regional refinement  
36 over East Asia to simulate an extreme precipitation event. The event is triggered by a typical  
37 wind shear in the lower layer of the Meiyu front in East China during 25-27 June 2012 of the  
38 East Asian summer monsoon season. The simulations are evaluated using ground observations  
39 and reanalysis data. The simulated distribution and intensity of precipitation are analyzed to  
40 investigate the sensitivity to model configuration, resolution, and physics parameterizations. In  
41 general, simulations using global uniform-resolution and variable-resolution meshes share  
42 similar characteristics of precipitation and wind in the refined region with comparable  
43 horizontal resolution. Further experiments at multiple resolutions reveal the significant impacts  
44 of horizontal resolution on simulating the distribution and intensity of precipitation and  
45 updrafts. More specifically, simulations at coarser resolutions shift the zonal distribution of the  
46 rain belt and produce weaker heavy-precipitation centers that are misplaced relative to the  
47 observed locations. In comparison, simulations employing 4 km cell spacing produce more  
48 realistic features of precipitation and wind. The difference among experiments in modeling  
49 rain belt features is found mainly due to the difference of simulated wind shear formation and  
50 evolution during this event. Sensitivity experiments show that cloud microphysics have  
51 significant effects on modeling precipitation at non-hydrostatic scales, but their impacts are  
52 relatively small compared to that of convective parameterizations for simulations at hydrostatic  
53 scales. This study provides the first evidence supporting the use of convection-permitting  
54 global variable-resolution simulations for studying and improving forecasting of extreme  
55 precipitation over East China, and motivates the need for a more systematic study of heavy  
56 precipitation events and impacts of physics parameterizations and topography in the future.

57

58

59

60

## 61 **1. Introduction**

62 Extreme precipitation receives great attention because of its potential for generating  
63 flood, landslide, and other hazardous conditions. East China, occupied by more than 70% of  
64 the total population of China, is one of the areas with the most frequent intense extreme  
65 precipitation around the world (Zhai et al., 2005; Li et al., 2016). The socioeconomic  
66 development in regions such as the Yangtze River Delta region (YRD) in East China is  
67 remarkably vulnerable to extreme precipitation, making accurate forecast of extreme  
68 precipitation of great importance. The spatiotemporal variations of extreme precipitation over  
69 East China and their possible causes and underlying mechanisms have been investigated in  
70 many previous studies using observations and models (e.g., Ding et al., 2008; Zhang H. et al.,  
71 2011; Li et al., 2013; Zhang Q. et al., 2015, 2017; Hui et al., 2015; Liu et al., 2015; Li et al.,  
72 2016; Lin and Wang, 2016; Zhao et al., 2016; Zheng et al., 2016). Zhang et al. (2017)  
73 established a relationship between the western North Pacific subtropical high (WNPSH) and  
74 precipitation over East China and explored the underlying processes. Liu et al. (2015) analyzed  
75 data from the meteorological stations in East China and found significant increases in heavy  
76 precipitation at both rural and urban stations during 1955-2011. This enhanced precipitation  
77 intensity in East China has been partly attributed to localized daytime precipitation events (Guo  
78 et al., 2017). Recently, a regional climate model was used to simulate the regional climate  
79 extremes of China and noted large sensitivity of the simulated summer heavy precipitation over  
80 East China to the choice of cumulus parameterizations (Hui et al., 2015).

81 Numerical modeling is an important tool for understanding the underlying mechanisms  
82 of extreme precipitation and predicting precipitation characteristics that contributes to  
83 environmental impacts. Although precipitation modeling has improved in the last decades,  
84 accurate prediction of extreme precipitation remains challenging because of the multiscale  
85 nonlinear interactions of processes that generate heavy rainfall (Fritsch et al., 2004; Zhang et  
86 al., 2011; Sukovich et al. 2014). Although not a panacea for weather and climate modeling  
87 (NRC, 2012), previous studies suggested that increasing grid resolution could significantly  
88 improve modeling of extreme precipitation because the impacts of topography, land-use, land-  
89 atmosphere interaction, and other important processes are better resolved (e.g., Giorgi and  
90 Mearns, 1991; Giorgi and Marinucci, 1996; Leung et al., 2003; Bacmeister et al. 2014;  
91 ECMWF2016). With advances in computing and numerical modeling, convection-permitting  
92 modeling offers even more hope for reducing biases in simulating precipitation as convection  
93 and the strong vertical motions that are key to generating extreme precipitation are more

94 explicitly resolved (Pedersen and Winther, 2005; Déqué et al., 2007; Gao et al., 2017; Yang et  
95 al. 2017; Prein et al., 2015, 2017). Previous studies suggested that convection-permitting  
96 modeling is needed for more accurate prediction of the timing, distribution, and intensity of  
97 extreme precipitation events over China (e.g., Zhang et al., 2013; Xu et al., 2015).

98 Most studies of convection-permitting simulations have adopted non-hydrostatic  
99 regional models developed for weather forecasting or regional climate modeling (Prein et al.  
100 2015). Global models capable of simulating non-hydrostatic dynamics are not as common as  
101 regional models, but they offer some advantages including the ability to provide global  
102 forecasts or simulations while avoiding numerical issues associated with lateral boundary  
103 conditions that are major sources of uncertainty in regional modeling and also limit regional  
104 feedback to large-scale circulation (e.g., Giorgi and Mearns, 1999; Wang et al. 2004; Laprise  
105 et al., 2008; Leung 2013; Prein et al. 2015). Non-hydrostatic global-variable resolution models,  
106 in particular, are useful as they allow convection-permitting simulations to be performed using  
107 regional refinement that significantly reduces computational cost compared to global  
108 convection-permitting modeling. Although global hydrostatic variable-resolution climate  
109 models, such as the variable-resolution version of Community Earth System Model, have been  
110 used in various applications in the last few years (e.g., Rauscher et al., 2013; Zarzycki et al.,  
111 2014, 2015; Rhoades et al., 2016; Huang et al., 2016; Wu et al., 2017; Gettelman, et al., 2018;  
112 Wang et al., 2018; Burakowski et al., 2019), so far few studies used global non-hydrostatic  
113 variable-resolution models to investigate weather or climate simulations, particularly at  
114 convection-permitting scales (e.g., Prein et al., 2015). This study explores the use of a non-  
115 hydrostatic global variable resolution model, the Model for Prediction Across Scales (MPAS)  
116 for modeling an extreme precipitation event in East China.

117 MPAS is a new multiscale modeling approach developed to take advantage of advances  
118 in mesh generation by employing the spherical centroidal Voronoi tessellations (SCVTs) (Du  
119 et al. 1999; Ringler et al. 2008). The SCVTs in MPAS enable local mesh refinement through  
120 the mesh generation process where a specified scalar density function determines higher and  
121 lower resolution regions in the mesh (see, e.g., Ju et al. 2011). Meshes can be configured with  
122 multiple high-resolution regions, and high resolution in one region does not need to be balanced  
123 by coarser resolution elsewhere. The underlying theory of SCVTs is robust concerning mesh  
124 properties and mesh generation. The atmospheric solver in MPAS (Skamarock et al, 2012)  
125 integrates the non-hydrostatic equations, and as such it is suitable for both weather and climate  
126 simulation, i.e. for both nonhydrostatic and hydrostatic flow simulation. MPAS has been  
127 evaluated and used in previous studies for investigating the resolution impact on modeling

128 clouds and precipitation (O'Brien et al., 2013; Zhao et al., 2016), the structure of the inter-  
129 tropical convergence zone (ITCZ) (Landu et al., 2014), precipitation extremes (Yang et al.,  
130 2014), atmospheric river frequency (Hagos et al., 2015), the position and strength of the eddy-  
131 driven jet (Lu et al., 2015), global atmospheric predictability at convection-permitting scales  
132 (Judt, 2018), and regional climate modeling (Sakaguchi et al., 2015, 2016). Except for Zhao et  
133 al. (2016) and Judt (2018), the aforementioned studies used a hydrostatic version of MPAS  
134 applied at resolutions ranging from ~25 km to 200 km.

135 To date, few studies have examined the MPAS performance in modeling extreme  
136 precipitation events, particularly at grid scales of ~10 km or less. In this study, we examine the  
137 MPAS performance in simulating a heavy precipitation event over the YRD region of East  
138 China and investigate its sensitivity to horizontal resolution and physics parameterizations. A  
139 heavy precipitation event that occurred on June 25-27 of 2012 over the YRD region of East  
140 China is selected as it is one of the ten heaviest precipitation events in 2012. This rainfall event  
141 was triggered by a typical southwest vortex in the middle and high troposphere and wind shear  
142 in the lower layer of Meiyu front over East China during the East Asian summer monsoon (e.g.,  
143 Xiang et al., 2013; Yao et al., 2017), initiated around 1200 UTC of 25 June. Most (more than  
144 two third) of heavy precipitation events over East China were caused by wind shear associated  
145 with the Meiyu front in recent decades (Yao et al., 2017). During this period, a heavy  
146 precipitating system propagated along the Yangtze River and produced as much as 244 mm of  
147 precipitation in 24 hours at some locations. The continuous precipitation led to 17 deaths and  
148 about RMB 3.68 billion in total damage, and affected more than 685 million people in the  
149 provinces of Central and East China. Simulations are performed using MPAS (v5.2) with  
150 different cumulus and microphysics schemes. We first compare simulations produced using a  
151 global mesh with uniform resolution and a global variable resolution mesh with a refined region  
152 that has the same resolution as that of the global uniform mesh. The goal is to demonstrate the  
153 fidelity of global variable resolution modeling relative to the more computationally expensive  
154 global high-resolution modeling approach in regions that share the same horizontal resolution.  
155 The impacts of resolutions at hydrostatic scales (with convective parameterizations) and non-  
156 hydrostatic scales (i.e., convection-permitting scales with convection processes largely  
157 resolved) are also examined. The MPAS simulations are evaluated against weather station  
158 observations from the National Meteorological Information Center of the China  
159 Meteorological Administration (CMA). In addition, the modeling results are also compared  
160 with the forecasts produced by the Global Forecast System (GFS) of the National Centers for  
161 Environmental Prediction (NCEP).

162           The rest of the paper is organized as follows. Section 2 describes briefly the MPAS  
163 model, the physics parameterizations, and the model configuration for this study, followed by  
164 a description of data for evaluation. The series of global uniform and variable resolution  
165 experiments are analyzed in section 3. The findings are then summarized in section 4.

166

## 167 **2. Data and methodology**

### 168 **2.1 Model and experiments**

#### 169 *2.1.1 MPAS-Atmosphere (MPAS-A) model*

170           This study uses a fully compressible non-hydrostatic model (MPAS v5.2) developed  
171 for weather prediction and climate applications. The non-hydrostatic dynamical core of MPAS  
172 is described in Skamarock et al. (2012). MPAS uses C-grid staggering of the prognostic  
173 variables and centroidal Voronoi meshes to discretize the sphere. The unstructured spherical  
174 centroidal Voronoi tessellation (SCVT) generation algorithms can provide global quasi-  
175 uniform resolution meshes as well as variable-resolution meshes through the use of a single  
176 scalar density function, hence opening opportunities for regional downscaling and upscaling  
177 between mesoscales and non-hydrostatic scales to hydrostatic scales within a global framework.  
178 The vertical discretization uses the height-based hybrid terrain-following coordinate (Klemp,  
179 2011), in which coordinate surfaces are progressively smoothed with height to remove the  
180 impact of small-scale terrain structures. The dynamical solver applies the split-explicit  
181 technique (Klemp et al., 2007) to integrate the flux-form compressible equations. The basic  
182 temporal discretization uses the third order Runge-Kutta scheme and explicit time-splitting  
183 technique (Wicker and Skamarock, 2002), similar to that used in the Weather Research and  
184 Forecasting (WRF) model (Skamarock et al., 2008). The scalar transport scheme used by  
185 MPAS on its Voronoi mesh is described in Skamarock and Gassmann (2011), and the  
186 monotonic option is used for all moist species. The extensive tests of MPAS using idealized  
187 and realistic cases verify that smooth transitions between the fine- and coarse-resolution  
188 regions of the mesh lead to no significant distortions of the atmospheric flow (e.g., Skamarock  
189 et al., 2012; Park et al., 2013).

190           In the current version (v5.2) of MPAS, there are a few physics schemes available. Three  
191 convective parameterizations can be used. The Kain-Fritsch (KF, Kain, 2004) and the new  
192 Tiedtke (NTD, Bechtold et al., 2004, 2008, 2014) schemes represent both deep and shallow  
193 convection using a mass flux approach with a convective available potential energy (CAPE)  
194 removal time scale (Kain, 2004). The third one, the GF scheme (Grell and Freitas, 2014), is

195 based on the Grell-Devenyi ensemble scheme (Grell and Devenyi, 2002) using the multi-  
 196 closure, multi-parameter, ensemble method but with improvements to smooth the transition to  
 197 cloud-resolving scales following Arakawa et al. (2011). This scale-awareness is critical for  
 198 global variable resolution simulation across hydrostatic (e.g., tens of km) and non-hydrostatic  
 199 scales (e.g., 4 km). Fowler et al. (2016) implemented the GF convective parameterization in  
 200 MPAS and examined the impacts of horizontal resolution on the partitioning between  
 201 convective-parameterized and grid-resolved precipitation using a variable-resolution mesh in  
 202 which the horizontal resolution varies between hydrostatic scales ( $\sim 50$  km) in the coarsest  
 203 region of the mesh to non-hydrostatic scales ( $\sim 3$  km) in the most refined region of the mesh.  
 204 For cloud microphysics, the WSM6 (Hong and Lim, 2006) and Thompson (Thompson et al.,  
 205 2008) schemes, both of which are bulk microphysical parameterizations, are selected and  
 206 compared. Both schemes include six hydrometeor species: water vapor, cloud water, rain,  
 207 cloud ice, snow, and graupel (Gettelman et al., 2019). The WSM6 scheme is a one-moment  
 208 prognostic parameterization, while the Thompson scheme includes a two-moment prognostic  
 209 parameterization for cloud ice and the single-moment parameterization for the other  
 210 hydrometeor species. The two schemes apply the same formula of gamma distribution of  
 211 hydrometeor species:  $N(D) = N_0 D^\mu e^{-\lambda D}$ , where  $D$  is the particle diameter,  $N_0$  is the intercept  
 212 parameter,  $\mu$  is the shape factor, and  $\lambda$  is the slope parameter, although the parameter values or  
 213 functions vary in the two schemes. The mass-size relationship in WSM6 and Thompson is also  
 214 expressed in the same formula as  $m(D) = aD^b$ . The mean falling speed is calculated as  
 215  $V(D) = cD^d (\frac{\rho_0}{\rho})^{0.5}$  in WSM6 and  $V(D) = cD^d (\frac{\rho_0}{\rho})^{0.5} \exp(-fD)$  in Thompson, respectively  
 216 (Hong and Lim, 2006; Thompson et al., 2008). In the formula, the WSM6 scheme assumes a  
 217 power-law fit between terminal velocity and particle size as Locatelli and Hobbs (1974), while  
 218 the Thompson scheme incorporates an exponential decay parameter to allow for a decrease in  
 219 falling speed with increasing size (Molthan et al., 2012). Two options are available for  
 220 representing the planetary boundary layer (PBL) processes, the Mellor-Yamada-Nakanishi-  
 221 Niino (MYNN) scheme (Nakanishi and Niino, 2006 and 2009) and the YSU scheme (Hong et  
 222 al., 2006; Hong 2010). This study used the MYNN scheme for the PBL processes. The Noah  
 223 scheme (Chen and Dudhia, 2001) and the RRTMG scheme (Mlawer et al., 1997; Iacono et al.,  
 224 2000) were implemented, respectively, for the land surface and radiative transfer processes.

225

### 226 2.1.2 Numerical experiments

227 In this study, the height coordinate of MPAS is configured with 55 layers, and the model  
228 top is at 30 km. Multiple experiments are conducted with MPAS using quasi-uniform  
229 resolution meshes and variable resolution meshes. Two quasi-uniform resolution meshes and  
230 three variable resolution meshes are configured, similar to those shown in Figure 1a and b that  
231 are coarsened to display the structure of the individual mesh cells. The quasi-uniform mesh has  
232 essentially the same mesh spacing globally, while the variable resolution mesh has finer mesh  
233 spacing in the refined region with a transition zone between the fine and coarse resolution  
234 meshes. More details about the mesh generation can be found in Ringler et al. (2011). The two  
235 quasi-uniform meshes have grid spacing that approximately equals to 15 km (U15km) and 60  
236 km (U60km). The three variable resolution meshes feature a circular refined high-resolution  
237 region centered over East China as shown in Figure 1c. Figure 1c shows the exact mesh size  
238 distribution of the 4-60km variable resolution mesh (V4km) that has a refined region with grid  
239 spacing of approximately 4 km, and the mesh spacing gradually increases through a transition  
240 zone to approximately 60 km for the rest of the globe. The other two variable resolution meshes  
241 (V16km and V30km) have a similar mesh structure as the V4km mesh but with a mesh spacing  
242 of 16 km and 30 km, respectively, over the refined region that gradually increases to 128 km  
243 and 120 km, respectively, elsewhere.

244 Experiments U15km and V16km are compared to examine the difference between  
245 global uniform and variable resolution simulations in capturing the precipitation in the refined  
246 region, in order to explore the potential of regional refinement for regional weather and climate  
247 simulation. It is noteworthy here that the U15km mesh comprises ~2.5 million cells and the  
248 V16km mesh only comprises ~0.11 million cells. The difference in the number of mesh cells  
249 leads to a difference in computational and storage demand. With the TH-2 supercomputer of  
250 National Supercomputer Center in Guangzhou (NSCC-GZ), it takes ~9000 CPU hours and  
251 ~240 CPU hours to finish a one-day simulation for U15km and V16km, respectively. In  
252 addition, with the standard MPASv5.2, the sizes of output data per one-day simulation for  
253 U15km and V16km are 0.5 T and 0.02 T, respectively. The same time step of 60 second is used  
254 for physics and dynamics for both U15km and V16km simulations. In order to investigate the  
255 potential impact from physics parameterizations, two available convective parameterizations  
256 (GF and NTD) are used for each experiment with the two meshes. Two cloud microphysics  
257 schemes (WSM6 and Thompson) are also tested, but the precipitation differences in the U15km  
258 and V16km experiments are small. Therefore, only the results using WSM6 with two different  
259 convective parameterizations are shown in this study for the two meshes (U15km.NTD,  
260 U15km.GF, V16km.NTD, and V16km.GF).

261 The U60km, V30km, V16km, and V4km experiments are conducted to quantify the impacts  
262 of horizontal resolution on simulating precipitation characteristics. The numbers of grid cells  
263 in the U60km, V30km, V16km, and V4km meshes are ~0.16 million, 0.10 million, ~0.11  
264 million, and ~0.8 million, respectively. Difference in the number of cell and minimum cell size  
265 also leads to a difference in computational and storage demand. With the TH-2 supercomputer  
266 of NSCC-GZ, it takes ~200 CPU hours, ~150 CPU hours, ~240 CPU hours, and ~1800 CPU  
267 hours to finish a one-day simulation for U60km, V30km, V16km, and V4km meshes,  
268 respectively. In addition, with the standard MPASv5.2, the sizes of output data per one-day  
269 simulation for the four meshes are 0.03 T, 0.02 T, 0.02 T, and 0.15 T, respectively. The time  
270 steps used for physics and dynamics for the four meshes are 300 seconds, 120 seconds, 60  
271 seconds, and 20 seconds, respectively.

272 As discussed above, GF is the only convective parameterization that has been tested  
273 with scale-aware capability for using across the hydrostatic (e.g., tens of km) and non-  
274 hydrostatic scales (e.g., 4 km). Therefore, in order to investigate the difference among the  
275 experiments with the four meshes (U60km, V30km, V16km, and V4km), they are all  
276 conducted with the GF convective parameterization. Since the cloud microphysics has  
277 significant impact on the V4km simulations (discussed latter), the experiments of V4km with  
278 both WSM6 (V4km.WSM6) and Thompson (V4km.Thompson) cloud microphysics schemes  
279 are analyzed in this study. When examining the difference between the global uniform and  
280 variable resolution simulations and investigating the impact of mesh spacing, the same physics  
281 schemes and parameter values are used in multiple experiments if not specified explicitly. All  
282 the numerical experiments discussed above are summarized in Table 1.

283 Due to the large computing cost and data storage of the experiments conducted,  
284 particularly for the U15km and V4km experiments, this study does not perform ensemble  
285 simulations. Instead, the bootstrapping statistical analysis is used to test the statistical  
286 significance of the difference among multiple experiments investigated in this study. The  
287 bootstrap method uses resampling technique to extract certain samples, called bootstrap  
288 samples, within the range of the original data. Statistical metrics, such as averages, variances,  
289 correlation coefficient, can be calculated for each bootstrap sample. For a given confidence  
290 level (e.g., 95%), bootstrap confidence intervals of specific statistical metric can be estimated  
291 (e.g., Efron, 1992; Efron and Tibshirani, 1994).

292 To simulate the heavy precipitation event that occurred during June 25-27 of 2012 over  
293 the YRD of East China, all the MPAS experiments were initialized at 0000 UTC of 23 June  
294 2012 to allow appropriate spin-up time, and the modeling results for 25-27 June 2012 are

295 analyzed. The simulations were initialized using the analysis data at 1° horizontal resolution at  
296 0000 UTC of 23 June 2012 from the Global Forecast System (GFS) of National Center for  
297 Environmental Prediction (NCEP), the same as that used by the GFS forecast for the period.  
298 The sea surface temperature (SST) is also prescribed the same as that used by the GFS forecast  
299 for the period. This way, the MPAS simulation results can also be compared against the GFS  
300 forecast starting from the 0000 UTC of 23 June 2012.

## 301 **2.2 Dataset**

302 Several datasets are used to evaluate the MPAS simulations. The hourly precipitation  
303 dataset from the National Meteorological Information Center of CMA is used for evaluating  
304 the simulated precipitation characteristics. In this dataset, the rainfall was measured by either  
305 tipping-buckets or self-recording siphon rain gauges, or from automatic rain gauges. The data  
306 were subject to strict three-step quality control by station, provincial, and national departments.  
307 The methods of quality control mainly include the checking of climate threshold value, extreme  
308 value, spatial and temporal consistency and the checking through human-computer interaction.  
309 All the data used in this study are quality-controlled. The distribution of stations over the study  
310 domain is shown as the color-filled circles in Figure 2. Over the YRD region of East China  
311 (25°N-36°N, 114°E-123°E, denoted as the black box in Fig. 2), there are 511 stations. The  
312 minimum and maximum distances between two stations are ~3 km and ~70 km, respectively,  
313 and the mean is ~25 km. The hourly wind field dataset from the ECMWF Reanalysis (ERA5)  
314 (0.28°×0.28°) (<https://rda.ucar.edu/datasets/ds630.0/>) is used as the reference for evaluating the  
315 simulated distributions of winds. Lastly, the global forecast products at 0.5° and 1° horizontal  
316 resolutions starting from UTC00 of 23 June 2012 are also used for comparison. The GFS  
317 forecast products are downloaded from [https://www.ncdc.noaa.gov/data-access/model-](https://www.ncdc.noaa.gov/data-access/model-data/model-datasets/global-forecast-system-gfs)  
318 [data/model-datasets/global-forecast-system-gfs](https://www.ncdc.noaa.gov/data-access/model-data/model-datasets/global-forecast-system-gfs) (last access on May 27 of 2019). Since the focus  
319 of this study is not to investigate the difference between MPAS and GFS or to evaluate the  
320 performance of GFS, details about the GFS are not discussed here but can be found on the  
321 website listed above.

322

## 323 **3. Results**

### 324 **3.1 Simulations at quasi-uniform and variable resolutions**

325 Figure 2 shows the spatial distributions of precipitation and wind at 850 hPa averaged  
326 during the event (June 25 00:00 to June 27 12:00 UTC Time) from the simulations with global  
327 uniform (15 km) and variable (16 km over East China) resolutions (U15km.NTD and

328 V16km.NTD). The mean precipitation from the CMA stations and the winds from the ERA-  
329 interim reanalysis are also shown. The CMA observations show average precipitation rate  
330 exceeding 50 mm/day over central East China with a heavy rain belt extending from west to  
331 east along 31°N. The rain belt is associated with the wind shear near the surface that is typically  
332 accompanied with the Meiyu front during the East Asian summer monsoon. In general, both  
333 simulations capture the observed precipitation pattern. It is evident that the modeling results  
334 over the refined region are consistent between the uniform and variable resolution simulations.  
335 The spatial correlation coefficient between the two simulations over the refined region (entire  
336 region shown in Fig. 2) is 0.85. Besides precipitation, both simulations also capture the  
337 distribution of winds from the reanalysis data. The wind fields between the two simulations are  
338 also consistent with a spatial correlation coefficient of 0.99.

339 As mentioned above, the precipitation during this event is concentrated in a west-east  
340 narrow belt. For a more quantitative comparison, Figure 3 shows the zonal averaged  
341 precipitation during the event over the YRD region of East China (25°N-36°N, 114°E-123°E,  
342 denoted as the black box in Fig. 2) from observations and simulations. The CMA observations  
343 show an evident precipitation peak reaching ~40 mm/day around the latitude of 31°N. All four  
344 simulations with different resolutions and convective parameterizations capture well the zonal  
345 distribution of observed precipitation. The correlation coefficients are 0.9 and 0.89 for the  
346 U15km and V16km simulations with the GF scheme, respectively, and 0.89 and 0.86 for the  
347 same simulations but with the NTD scheme. This comparison further indicates that the  
348 simulations at global uniform and variable resolutions are consistent with each other, and the  
349 different convective parameterizations only have negligible impact on this consistency.  
350 Although this consistency does not depend on the convective schemes, simulations with the  
351 GF parameterization produce larger peak precipitation than those with the NTD  
352 parameterization and are more consistent with observations for this event. The impact of cloud  
353 microphysics (WSM6 and Thompson) on the consistency in modeling total precipitation is also  
354 examined and is found to be negligible (Fig. S1 and S2 in the supporting materials), although  
355 there are some impacts on the simulated grid-resolved precipitation (Fig. S3 in the supporting  
356 material).

357 Figure 4 shows the meridional precipitation propagation over East China (denoted as  
358 the black box in Fig. 2) during the event. The CMA observations indicate that the rain belt  
359 propagates from 26°N at 06 UTC of 25 June to 31°N at 00 UTC of 26 June and includes two  
360 precipitation peaks around 31°N. The rainfall reaches the first peak around 00 UTC of 26 June.

361 The rain belt stays around 31°N and reaches the second peak around 00 UTC of 27 June. The  
362 event ends around 12 UTC of 27 June (Fig. S4 in the supporting material). The first  
363 precipitation peak was generated by the southwest-northeast wind shear line formed over  
364 Central East China along with a vortex over the Southwest at 00 UTC of 26 June. The shear  
365 line gradually extended eastward, leading to the second precipitation peak around 00 UTC of  
366 27 June (Fig. S5 in the supporting material). All four experiments generally simulate the  
367 southwest vortex and wind shear during the event, although the strength and location do not  
368 match perfectly with the reanalysis. As the large-scale environment is quite well represented  
369 in the model, the simulations also generally capture the two peaks of precipitation along 31°N  
370 as observed. However, both U15km and V16km simulate a broader rain belt, resulting in  
371 positive biases of precipitation south of 30°N (Fig. S6 in the supporting materials). Both  
372 simulations shift the first peak precipitation southward. In addition, the simulations extend the  
373 first peak precipitation period and shorten the second one to some extent (Fig. S6 in the  
374 supporting materials). The lower averaged total precipitation around 31°N from the simulation  
375 with the NTD parameterization (Fig. 3) is mainly due to the lower rainfall before 26 June  
376 compared to the one with the GF parameterization (Fig. S6). For the two precipitation peaks,  
377 the simulation with NTD is comparable to the one with GF. Although the two convective  
378 parameterizations lead to significant difference in simulating total precipitation before 26 June,  
379 both simulations generate consistent wind circulations at 700 hPa before 26 June with spatial  
380 correlation coefficients above 0.9 (over the domain as shown in Fig. S5 in the supporting  
381 material). Although the two convective parameterizations lead to different total precipitation,  
382 they have negligible impact on the consistency in modeling precipitation propagation using  
383 uniform and variable resolutions during this event. The correlation coefficients are 0.48 and  
384 0.42 for the simulations with the GF scheme at the resolutions of U15km and V16km,  
385 respectively, and 0.55 and 0.54 for the simulations with the NTD scheme at the two resolutions.  
386 The results again indicate the consistency between the simulations at the global uniform and  
387 variable resolutions at hydrostatic scale over the refined region regardless of the convective  
388 parameterization used.

389 Overall, for the selected event, the MPAS simulations at global uniform and variable  
390 resolutions produce consistent results over the refined region with comparable horizontal  
391 resolution in terms of the spatial patterns of precipitation and wind fields and the precipitation  
392 propagation. This finding is in general agreement with the findings by previous studies of  
393 MPAS with idealized experiments (e.g., Zhao et al., 2016) and real-world experiments (e.g.,

394 Sakaguchi et al., 2015). These findings provide the basis for using global variable resolution  
395 configurations of MPAS for modeling extreme precipitation over East China. In the following,  
396 the impacts of resolution on modeling extreme precipitation during this event are investigated  
397 with multiple global variable-resolution experiments.

398

## 399 **3.2 Impacts of resolution**

### 400 *3.2.1 Parameterized and resolved precipitation*

401 Multiple experiments using MPAS at various resolutions are conducted as stated in the  
402 methodology section. The resolution crosses the scales from 60 km, 30 km, 16 km to 4 km. For  
403 global variable resolution configurations, a scale-aware convective parameterization is needed,  
404 especially for the configuration that crosses the hydrostatic (convective parameterization is  
405 required) and non-hydrostatic scales (convection-permitting). Therefore, the experiments  
406 analyzed below are all conducted with the GF scheme that is developed for simulations down  
407 to ~ 4 km resolution (details can be found in Grell and Freitas, 2014). To demonstrate the scale-  
408 aware performance of the GF convective parameterization across various resolutions, Figure 5  
409 shows the spatial distributions of convective parameterized and resolved precipitation averaged  
410 during the event. At the resolution of 60 km and 16 km, precipitation produced from the  
411 convective parameterization dominates the total precipitation amount. On the contrary, at the  
412 resolution of 4 km, the total precipitation amount from simulations with two different  
413 microphysics is dominated by the resolved precipitation. The fraction of parameterized  
414 precipitation in the total decreases significantly from the simulations at 16 km to the ones at  
415 4km over the heavy precipitation region (Fig. S7 in the supporting materials). It is also  
416 interesting that the fraction of parameterized precipitation increases from the simulations at 60  
417 km to the ones at 16 km to some extent. This demonstrates that the GF scheme is aware of the  
418 resolution change so the precipitation from the simulations at convection-permitting scale is  
419 mostly produced by the cloud microphysics in MPAS.

### 420 *3.2.2 Spatial and temporal variation*

421 Figure 6 shows the observed and simulated spatial distributions of precipitation and  
422 wind fields at 850 hPa averaged during the event. For comparison, the GFS forecast results at  
423 the resolutions of 1.0 degree and 0.5 degree are also included. The GFS forecast results from  
424 the two resolutions are similar, both showing a northward shifted rain belt compared to the  
425 CMA observation. Due to the northern shift of the rain belt, the spatial correlation coefficients  
426 between the GFS and the CMA observations over the entire region of Fig. 6 are only 0.06 and

427 0.03 for the resolutions of 1.0 degree and 0.5 degree, respectively. In comparison, the spatial  
428 correlation coefficients between the CMA observations and the MPAS simulations at the  
429 resolutions of 60 km, 30 km, and 16 km are 0.49, 0.47, and 0.56, respectively. The correlation  
430 coefficients for the 4 km simulations with the WSM6 and Thompson microphysics schemes  
431 are 0.63 and 0.54, respectively. In general, the experiments at the convection-permitting scale  
432 (4 km) capture better the observed precipitation pattern than simulations with convective  
433 parameterization over the refined region, although the performance is affected by the  
434 microphysics scheme to some extent. On average of the entire region as shown in Fig. 6, all  
435 the simulations overestimate the observed precipitation with the mean biases ranging from  
436 +0.59 mm/day to +5.11 mm/day (Table 2).

437 In order to test the statistical significance of the difference in spatial distributions  
438 among the experiments, the 95% confidence intervals of spatial correlation are estimated based  
439 on the bootstrap analysis. Although the correlation coefficients estimated above have an  
440 uncertain range, at the 95% confidence level the results still indicate that the V16km simulation  
441 produces better spatial pattern of precipitation than other hydrostatic-scale simulations. In  
442 addition, the simulation at the convection-permitting scale is comparable to, if not better than,  
443 the V16km simulation. The results are summarized in Table 3. It is noteworthy that, although  
444 the difference in precipitation over East China is significant among the GFS forecasts at 0.5°  
445 and 1.0° resolutions and MPAS at various resolutions, their global distributions of precipitation  
446 and wind averaged during the event period are similar with spatial correlation coefficients of  
447 0.40-0.43 (precipitation) and 0.86-0.93 (wind), respectively, against the satellite retrieved  
448 precipitation and ERA5 reanalysis wind (Fig. S8 in the supporting material).

449 The zonal distributions of precipitation can better demonstrate the difference among  
450 the simulations. Figure 7 shows the observed and simulated zonal distributions of precipitation  
451 averaged during the event over the YRD region of East China. For comparison, the GFS  
452 forecasts at 1° and 0.5° resolutions are also included. The modeling results are sampled at the  
453 CMA stations. Consistent with the spatial distributions of precipitation shown in Fig. 6, the  
454 GFS forecasts at both 0.5° and 1.0° resolutions reproduce the precipitation peak of ~40 mm/day  
455 but shift the rain belt northward by about 4.0° latitude from 31°N to 35°N. The MPAS  
456 simulations at 16 km and 30 km with the GF scheme can well capture the peak precipitation  
457 around 31°N, although the simulation at 30 km produces a second lower peak of precipitation  
458 around 29°N. The simulation at 60 km produces much lower precipitation peak of ~25 mm/day  
459 and shifts the rain belt southward to around 30°N. The underestimate of the simulation at 60

460 km is mainly due to the underestimate of the convective parameterized rain (Fig. 5). It is  
461 noteworthy that on regional average the simulation at 60 km overestimates the observed  
462 precipitation with the mean bias of +2.18 mm/day (Table 2). For the two MPAS simulations at  
463 4 km, the precipitation is mainly generated by cloud microphysics (Fig. 5) and therefore can  
464 be significantly affected by the cloud microphysics schemes. The MPAS simulations at 4 km  
465 with WSM6 and Thompson produce different zonal distributions of the rain belt. The  
466 simulation using WSM6 reproduces the peak of precipitation, while the simulation using  
467 Thompson produces higher precipitation with a peak at 50 mm/day and shifts the peak  
468 northward by about 1 degree. The simulation at 4 km with the Thompson scheme has much  
469 higher positive bias than the one with the WSM6 scheme (Table 2). Overall, the correlation  
470 coefficients between the CMA observations and the GFS forecasts are -0.19 and -0.15 for 0.5°  
471 and 1.0°, respectively, and the correlation coefficients are 0.68, 0.71, 0.89, and 0.97 (0.72) for  
472 the MPAS simulations at 60 km, 30 km, 16 km, and 4 km with the WSM6 (Thompson) cloud  
473 microphysics. At the 95% confidence level, the difference among the experiments is significant  
474 (Table 3).

475 Figure 8 compares the observed and simulated precipitation propagation during the  
476 event over East China. The modeling results are sampled at the CMA stations. The GFS  
477 forecasts at 0.5° and 1.0° are similar, and both generate a heavy precipitation zone between  
478 34°N and 35°N that lasts for about 18 hours from UTC12 of June 26. This is largely different  
479 from the CMA observations, so the correlation coefficients between the forecasts and  
480 observations are only 0.02 and 0.03 for 0.5° and 1.0°, respectively. The northward shift of rain  
481 belt during the event (shown in Fig. 6 and 7) is related to the GFS forecast that only produced  
482 the second peak of precipitation around UTC 0000 of 27 June while totally missing the first  
483 peak (Fig. S9). In addition, the GFS forecast overestimates the second peak and shift it towards  
484 the north by about 4°. The timing and location shift of the rain belt in the GFS forecast are  
485 mainly because of the bias of GFS in simulating the wind shear in this event. The GFS forecast  
486 failed to produce the southwest-northeast wind shear line around UTC 0000 of 26 June and  
487 generated too broad vortex over the west. Around UTC 0000 of 27 June, GFS simulated the  
488 wind shear line but locating it further north (Fig. S10 in the supporting material).

489 The MPAS simulations are highly dependent on the resolutions. All simulations  
490 roughly produce the two peaks of precipitation as observed during the event. However, the  
491 experiment at 60 km simulates the first precipitation peak southward and the second peak  
492 northward of the observations, while the experiment at 30 km simulates the second peak further

493 south and a few hours earlier. The time and location shift corresponding well to biases in  
494 simulated wind shear (Fig. S10). The spatial correlation coefficients of precipitation are 0.30  
495 and 0.32 between the observations and the simulations at 60 km and 30 km, respectively. The  
496 experiments at 16 km and 4 km with the WSM6 cloud microphysics scheme can better capture  
497 the timing and latitude of the observed precipitation event than U60km and V30km (Fig. S11  
498 in the supporting materials), however both V16km and V4km overestimate the first peak  
499 precipitation and underestimate the second peak. The experiment at 4 km with the Thompson  
500 scheme overestimates the precipitation amount of both peaks. Overall, all the simulations  
501 overestimate the observed precipitation during the event (Table 2). The correlation coefficients  
502 are 0.41 and 0.42 (0.38) for 16 km and 4 km with the WSM6 (Thompson) cloud microphysics  
503 schemes, respectively. At the 95% confidence level (Table 3), the experiments at 16 km and 4  
504 km are comparable in terms of simulating the propagation of this rain belt and better than the  
505 experiments at other resolutions. It is interesting to note that MPAS and GFS forecasts, sharing  
506 the same initial condition, simulate different large-scale circulation particularly the wind shear  
507 structure with the system evolving (Fig. S10). The model capability in successfully capturing  
508 the wind shear structure during this event determines the performance in generating the rain  
509 belt evolution. The formation and evolution of wind shear during the Meiyu front over East  
510 China have been found interacting with multiscale processes and systems, including terrain and  
511 convective latent heat (Yao et al., 2017). Different representation of the terrain over East China  
512 in various resolutions may impact the simulated wind shear structure. Previous studies also  
513 found that convective latent heat may vary with resolutions and physics (Hagos et al., 2013;  
514 Zhao et al., 2016), which can further affect the simulation of wind shear structure. Therefore,  
515 the difference in resolution and physics between MPAS and GFS may result in their difference  
516 in simulating the formation and evolution of wind shear structure during the event. A more  
517 detailed exploration of the differences between the MPAS and GFS simulations is beyond the  
518 scope of this study.

519         The spatial distribution of the rain belt can also be reflected by the vertical wind  
520 distributions. Figure 9 compares the height-latitude cross section of the winds averaged over  
521 the region (shown as in Fig. 6) during the event from the ERA5 reanalysis, the GFS forecasts,  
522 and the MPAS simulations. In the ERA5 reanalysis wind fields, vertical motion is located  
523 primarily around 31°N, extending from the lower troposphere (~900 hPa) to the upper  
524 troposphere (~200 hPa). The GFS simulates the vertical motion primarily around 33°N, but the  
525 vertical motion is also strong around 35°N from 600 hPa to 200 hPa, which can be linked to

526 the heavy precipitation generated there. These biases result in weaker correlation in vertical  
527 winds between the reanalysis and the GFS forecasts with coefficients of 0.29 and 0.32 for 0.5°  
528 and 1.0° resolutions, respectively. The MPAS experiment at 60 km simulates the vertical  
529 motion toward the south around 28°N. The MPAS experiments at 30 km and 16 km generally  
530 agree well with the ERA5 reanalysis, although both generate higher vertical motion in the south  
531 (e.g. 25°N) to some extent. The correlation coefficients between the reanalysis and the MPAS  
532 experiments at 60 km, 30 km, and 16 km are 0.53, 0.68, and 0.80, respectively. The MPAS  
533 experiment at 4 km with the WSM6 scheme produces consistent vertical motion with that in  
534 the ERA5 reanalysis, while the one with the Thompson scheme shifts the vertical motion a  
535 little further north. Both experiments at 4 km have the highest correlation in the distributions  
536 of vertical motion with the reanalysis with coefficients of 0.85 and 0.80 for WSM6 and  
537 Thompson, respectively. The statistical significance tests based on the bootstrap analysis  
538 indicate that at the 95% confidence level the model performance at 16 km and 4 km in terms  
539 of simulating vertical structure of winds are comparable and better than the simulations at  
540 coarser resolution (Table 3). The zonal distributions of precipitation discussed above  
541 correspond well with the distributions of vertical motion in all the experiments. Differences in  
542 the spatial distribution of vertical motions suggest that model resolution, and in some degree  
543 cloud microphysics parameterizations, have important effects on simulating the structure of the  
544 wind shear over East China during the East Asian summer monsoon and the embedded  
545 precipitation.

546

### 547 *3.2.3 Distribution of extreme precipitation*

548 Besides predicting the spatial and temporal variations of the rain belt, it is also critical  
549 to capture the location and intensity of extreme precipitation within the heavy rain belt. Since  
550 the GFS forecasts shift the entire rain belt northward, only the MPAS simulations are analyzed  
551 here. Figure 10 shows the spatial distributions of precipitation averaged during the event over  
552 the heavy rain region (27°N-32°N and 110°E-122°E). The CMA observations show that heavy  
553 precipitation exceeding 50 mm/day mainly occurs over the plains of South Anhui province and  
554 Southeast Hubei province and part of the Huang Mountains. The MPAS experiment at 60 km  
555 simulates much smaller areas with heavy precipitation exceeding 50 mm/day. In addition, it  
556 simulates heavy precipitation over some areas of Hunan province, which is not observed by  
557 the CMA stations. The experiment at 30 km produces more numerous areas with heavy  
558 precipitation and captures the locations of heavy precipitation over the Huang Mountains.

559 However, it misses the heavy precipitation over the plains of South Anhui province and  
560 Southeast Hubei province; instead, it produces heavy precipitation over large areas of  
561 mountainous regions over Hunan and Jiangxi provinces. The experiment at 16 km simulates  
562 better spatial distribution of heavy precipitation, particularly capturing the heavy precipitation  
563 over the Huang Mountains and the plain of South Anhui province, although it still shifts the  
564 heavy precipitation from Southeast Hubei province to Hunan province. The experiments at 4  
565 km are affected by the cloud microphysics. The 4 km experiment with the WSM6 scheme  
566 produces the best spatial distribution among the MPAS experiments. It generally captures the  
567 observed heavy precipitation areas during this event as discussed above, although the locations  
568 do not perfectly match that of the observations. On the other hand, the 4 km experiment with  
569 the Thompson microphysics produces more areas of heavy precipitation over Central Anhui  
570 province. As a result, the correlation coefficients between the observations and the MPAS  
571 experiments at the resolutions of 60 km, 30 km, 16 km, and 4 km are 0.20, 0.21, 0.29, 0.50  
572 (WSM6), and 0.42 (Thompson), respectively. The statistical significance test based on the  
573 bootstrap analysis indicates that at the 95% confidence level the simulations at 4 km can better  
574 capture the spatial distribution of heavy precipitation than the simulations at resolutions of  
575 hydrostatic scale (Table 3). On average of the entire region as shown in Fig. 10, all the  
576 simulations overestimate the observed precipitation with the mean biases ranging from +2.28  
577 mm/day to +7.43 mm/day, except the simulation at 60 km with a small negative mean bias  
578 (Table 2). The simulation at 4 km with the WSM6 scheme has the smallest positive bias.

579 Figure 11 shows the probability density functions (PDFs) of hourly precipitation at all  
580 the CMA stations over East China during the event. The simulations are sampled at the CMA  
581 stations. Precipitation above  $\sim 5$  mm/hour ( $\sim 120$  mm/day) is considered very heavy and extra  
582 heavy storm rain event (refer to the CMA definition) that may cause dramatic flooding and  
583 damage locally or regionally. During this event, for precipitation lower than  $\sim 5$  mm/hour, the  
584 MPAS simulations at hydrostatic scales (60 km, 30 km, and 16 km) overestimate the frequency,  
585 while above  $\sim 5$  mm/hour, these simulations significantly underestimate the frequency. In  
586 contrast, the MPAS simulations at convection-permitting scale (4 km) produce much higher  
587 frequency of extreme precipitation above  $\sim 5$  mm/hour, more consistent with the observations.  
588 However, the simulated frequency of extreme precipitation at convection-permitting scale  
589 depends on the cloud microphysics schemes. Although the simulations at convection-  
590 permitting scale with both microphysics schemes overestimate the extreme precipitation ( $> 10$   
591 mm/hour), the Thompson scheme produces much higher frequency of extreme precipitation  
592 than the WSM6 scheme and results in a larger positive bias relative to the observations during

593 this event, which deserves further investigation in future. The coverage of observational  
594 stations with the mean distance of  $\sim 25$  km between each other over the study area may not be  
595 enough and results in the missing of some extreme precipitation, which may contribute partly  
596 to the positive biases of simulations. However, since the simulations are sampled at the CMA  
597 stations, the inconsistency of comparison between observation and simulation should be  
598 reduced, particularly at the scale of 4 km. The results also indicate that the convective  
599 parameterization appears not to be able to produce the higher intensity precipitation.

600 Previous studies found that the distribution of extreme precipitation correlates well with  
601 that of the lower tropospheric upward vertical velocity (e.g., Zhao et al., 2016). Figure 12 shows  
602 the PDFs of hourly upward vertical velocity averaged below 700 hPa at all the CMA stations  
603 during the event from the MPAS simulations. In general, the comparison of lower-level upward  
604 vertical velocity among the experiments is consistent with that of precipitation (Fig. 11) in  
605 those simulations at hydrostatic scales (i.e., 60 km, 30 km, and 16 km in this study) produce  
606 higher frequencies of updrafts  $< 4$  cm/s than simulations at 4 km and vice versa for stronger  
607 updrafts. The difference in updrafts between the 4 km MPAS simulations with two different  
608 cloud microphysics schemes is negligible. Another analysis with the simulated updrafts at  
609 various resolutions all regridded to  $0.5^\circ$  resolution shows the similar PDFs as Fig. 12. Previous  
610 studies have proposed some mechanisms underlying the resolution impacts on modeling  
611 vertical velocity (e.g., Rauscher et al., 2016; Jeevanjee et al., 2017; Herrington and Reed, 2017;  
612 O'Brien et al., 2016; Fildier et al., 2018). Among these mechanisms, Rauscher et al. (2016)  
613 argued that the resolution-dependent vertical velocity is caused by the interaction between the  
614 constraint of fluid continuity and macro-scale turbulence. They suggested that the vertical  
615 velocity should be more intense at higher resolution because the horizontal velocity increment  
616 follows approximately a power law of resolution. Therefore, the resolved vertical transport  
617 must increase as grid spacing decreases. Assuming atmospheric moisture is relatively  
618 insensitive to resolution, the upward moisture flux should increase as grid spacing decreases,  
619 hence producing more precipitation.

620 Figure 13 shows the PDFs of the upward moisture flux and the relationship between  
621 hourly precipitation versus upward moisture flux at 850hPa during the event from the MPAS  
622 simulations at 60km, 30km, 16km and 4km. It is evident that the simulations at higher  
623 resolutions produce more frequent intense upward moisture fluxes at 850hPa, consistent with  
624 Rauscher et al. (2016) and O'Brien et al. (2016). Rauscher et al. (2016) found a linear  
625 relationship between precipitation and upward moisture fluxes at lower level. The relationship

626 lines from this study as shown in Fig. 13 parallel the 1:1 reference line for all resolutions.  
627 However, the lines are consistently below the reference line for the convection-permitting  
628 simulations (4km) and are above the reference line for the hydrostatic simulations with  
629 convective parameterization (e.g., 16km, 30km, 60km). The simulated precipitation can be  
630 larger than the lower level upward moisture fluxes at hydrostatic scale because part of the  
631 precipitation is contributed by the convective parameterization rather than contributed by the  
632 resolved upward moisture flux (Rauscher et al., 2016). On the contrary, precipitation could be  
633 lower than the upward moisture flux at convection-permitting scale (e.g., 4km) as moisture is  
634 removed from cloud updrafts due to detrainment (e.g., O'Brien et al., 2016). Overall, our results  
635 of the resolution-dependent updraft and precipitation are consistent with Rauscher et al. (2016)  
636 and O'Brien et al. (2016).

637

#### 638 **4. Summary and discussion**

639 In this study, a series of MPAS simulations of a heavy precipitation event over East  
640 China, triggered by a typical southwest vortex in the middle and high troposphere and wind  
641 shear in the lower layer of the Meiyu front during the East Asian summer monsoon, are  
642 compared. The simulations are performed at various resolutions from hydrostatic (60 km, 30  
643 km, 16 km) to non-hydrostatic (4 km) scales. Consistency between the MPAS simulations at  
644 global uniform and variable resolutions is also investigated. Besides the impacts of resolution  
645 on simulating heavy precipitation, the impacts of convective and cloud microphysics schemes  
646 are also examined. All the MPAS simulations are evaluated using the CMA station  
647 observations of precipitation and the ERA5 reanalysis of winds, and compared against the  
648 NCEP GFS forecasts that share the same initial condition of the MPAS simulations.

649 In general, the MPAS simulations at global uniform (U15km) and variable (V16km)  
650 resolutions produce similar results in terms of the spatial and temporal distributions of  
651 precipitation and winds inside the refined region over East China. Both experiments can  
652 capture the observed precipitation characteristics. This suggests that the global variable-  
653 resolution configuration of MPAS may be appropriate to simulate heavy precipitation over East  
654 China, which is also consistent with the finding from previous studies using variable resolution  
655 MPAS with regional refinement over other parts of the globe (e.g., Sakaguchi et al., 2015; Zhao  
656 et al., 2016). The simulations with two different convective parameterizations show that the  
657 MPAS simulated distributions of precipitation are affected by the convective schemes at  
658 hydrostatic scales, while the impacts from the cloud microphysics schemes are small.

659           The variable-resolution simulations spanning hydrostatic and non-hydrostatic scales  
660 reveal that the scale-aware GF convective parameterization produces less convective  
661 parameterized precipitation as the horizontal resolution increases. Comparison against the  
662 station observations indicates that the MPAS simulations at 16 km and 4 km can generally  
663 better capture the observed temporal and zonal distribution of the rain belt in the simulated  
664 event than the simulations at coarser resolutions. The experiments at 4 km can better capture  
665 the areas with heavy precipitation ( $> 50$  mm/day) than the experiments at coarser resolutions  
666 compared to the observations, although the simulations at 4 km overestimate the first peak  
667 precipitation and underestimate the second one. This may indicate that the convective  
668 parameterization appears not to be able to produce intense precipitation. The analysis also  
669 shows that the underestimation of intense precipitation is consistent with the underestimation  
670 of resolved upward motions in the simulations at coarser resolutions. The biases in the locations  
671 of rain belt are mainly due to failure of the model to simulate the wind shear structure of the  
672 Meiyu front during this event. This suggests that the position and structure of the wind shear  
673 of the Meiyu front that produces the vertical motion is sensitive to the models and their specific  
674 configurations even though all simulations share the same initial condition. Previous studies  
675 have found that the formation and evolution of wind shear during the Meiyu front can interact  
676 with multiscale processes and systems over East China, including terrain and convective latent  
677 heat (Yao et al., 2017). Therefore, different representation of the terrain over East China in  
678 various resolutions and convective latent heat resulted from different physics schemes may  
679 affect the simulated wind shear structure among the MPAS experiments at various resolutions  
680 and between MPAS and GFS.

681           The performance of MPAS at convection-permitting scale is quite sensitive to the cloud  
682 microphysics scheme in terms of the distribution and intensity of extreme precipitation. This  
683 is consistent with Feng et al. (2018), who found that cloud microphysics parameterizations in  
684 convection permitting regional simulations have important effects on macroscale properties  
685 such as the lifetime, precipitation amount, stratiform versus convective rain volumes of  
686 mesoscale convective systems in the U.S. They attributed the impacts to the representation of  
687 ice phase hydrometeor species that influence the mesoscale convective systems through their  
688 influence on the diabatic heating profiles that provide dynamical feedback to the circulation  
689 (Yang et al. 2017). Hence more efforts may be needed to improve cloud microphysics  
690 processes for modeling extreme precipitation at convection-permitting scale in the future. In  
691 the meantime, aerosols have been found to play a critical role in simulating some heavy  
692 precipitation events over China through their impacts on cloud microphysics and/or radiation

693 (e.g., Zhong et al., 2015, 2017; Fan et al., 2015). The current version of MPAS does not  
694 represent aerosol-radiation and aerosol-cloud interactions, which may also contribute to the  
695 biases of extreme precipitation at convection-permitting scales. Lastly, it is also noteworthy  
696 that the resolution of 4 km may still be insufficient to resolve some convective cells, which  
697 may also contribute to the modeling biases (Bryan and Morrison, 2012).

698 This study provides the first evidence supporting the use of global variable resolution  
699 configuration of MPAS for simulating extreme precipitation events over East China. In  
700 particular, the MPAS variable-resolution experiment at convection-permitting scale (4 km)  
701 improves the simulated distribution and intensity of precipitation over the area of interest,  
702 which is consistent with previous studies using regional convection permitting models (e.g.,  
703 Zhang et al., 2013; Prein et al., 2015; Yang et al. 2017; Gao et al. 2017; Feng et al. 2018). The  
704 higher resolution MPAS experiments simulate better spatial distribution of heavy precipitation  
705 over the complex topographic region of East China, which suggests that topography may play  
706 a critical role and deserves further investigation in the future. Our results show that cloud  
707 microphysics parameterizations have important effects in convection permitting simulations,  
708 but modeling of other physical processes such as boundary layer turbulence, radiation, and  
709 aerosols may also affect the skill of convection permitting simulations. The GFS forecasts  
710 analyzed in this study show significant biases in precipitation distribution. The zonal shift of  
711 the rain belt by the MPAS simulations at coarser resolutions compared to simulations at finer  
712 resolutions suggests that resolution may have contributed to the GFS forecast biases. A more  
713 detailed exploration of the differences between the MPAS and GFS simulations is beyond the  
714 scope of this study.

715 Previous studies (Xue et al., 2007; Clark et al. 2016) noted the importance of ensemble  
716 simulations in predicting heavy precipitation. Due to the computational limitation, only one set  
717 of experiments with different physics and resolutions are evaluated in this study. The MPAS  
718 simulations of heavy precipitation with different initial conditions and refinement sizes deserve  
719 more evaluations. Finally, some studies noted that convection-permitting modeling does not  
720 always add values in simulating heavy precipitation compared to hydrostatic scale modeling  
721 (e.g., Kain et al., 2008; Rhoades et al., 2018; Xu et al., 2018). Rhoades et al. (2018) found that  
722 the improvement by increasing resolution may also depend on cloud microphysics  
723 parameterization. Increasing horizontal resolution alone sometimes can even lead to worse  
724 model performance. The impacts of increasing horizontal resolution on the overall model  
725 performance in simulating extreme precipitation may also be affected by the model structure  
726 and coupling among model components and processes (Jeevanjee et al., 2016; O'Brien et al.,

727 2016; Herrington et al., 2017, 2018; Gross et al., 2018). This study also found some sensitivity  
728 of modeling extreme precipitation to cloud microphysics, particularly at convection-permitting  
729 scale. More events of heavy precipitation over East China should be investigated in the future  
730 to more systematically evaluate the MPAS variable-resolution modeling framework and the  
731 impacts of resolution and physical parameterizations.

732

### 733 **Code availability**

734 The MPAS release v5.2 can be obtained at *mpas-dev.github.io*. Global meshes generated for  
735 the experiments used in this study are available upon request by contacting the corresponding  
736 author.

737

### 738 **Author contributions**

739 CZ and YW designed research. MX performed the simulations. CZ, MX, MZ, and ZH analyzed  
740 the simulations. JG collected and analyzed the observations. CZ, MX, and YW wrote the paper.  
741 LRL, MD, and WS guided the experiment design and edited the paper.

742

### 743 **Acknowledgements**

744 This research was supported by the Ministry of Science and Technology of China under grant  
745 2017YFC1501401 and the Fundamental Research Funds for the Central Universities. The  
746 study used computing resources from the High-Performance Computing Center of University  
747 of Science and Technology of China (USTC) and the TH-2 of National Supercomputer Center  
748 in Guangzhou (NSCC-GZ). Leung was supported by the U.S. Department of Energy Office of  
749 Science Biological and Environmental Research as part of the Regional and Global Modeling  
750 and Analysis program. PNNL is operated for the Department of Energy under contract DE-  
751 AC05-76RL01830.

752

753 **Reference**

- 754 Arakawa, A., Jung, J. H., & Wu, C. M.: Toward unification of the multiscale modeling of the  
755 atmosphere. *Atmospheric Chemistry and Physics*, 11(8), 3731-3742.  
756 <https://doi.org/10.5194/acp-11-3731-2011>, 2011.
- 757 Bacmeister, J. T., Wehner, M. F., Neale, R. B., Gettelman, A., Hannay, C., Lauritzen, P. H., ...  
758 & Truesdale, J. E.: Exploratory high-resolution climate simulations using the  
759 Community Atmosphere Model (CAM). *Journal of Climate*, 27(9), 3073-3099.  
760 <https://doi.org/10.1175/JCLI-D-13-00387.1>, 2014.
- 761 Bechtold, P., Chaboureau, J. P., Beljaars, A., Betts, A. K., Köhler, M., Miller, M., &  
762 Redelsperger, J. L.: The simulation of the diurnal cycle of convective precipitation over  
763 land in a global model. *Quarterly Journal of the Royal Meteorological*  
764 *Society*, 130(604), 3119-3137. <https://doi.org/10.1256/qj.03.103>, 2004.
- 765 Bechtold, P., Köhler, M., Jung, T., Doblas-Reyes, F., Leutbecher, M., Rodwell, M. J., ... &  
766 Balsamo, G.: Advances in simulating atmospheric variability with the ECMWF model:  
767 From synoptic to decadal time-scales. *Quarterly Journal of the Royal Meteorological*  
768 *Society*, 134(634), 1337-1351. <https://doi.org/10.1002/qj.289>, 2008.
- 769 Bechtold, P., Semane, N., Lopez, P., Chaboureau, J. P., Beljaars, A., & Bormann, N.:  
770 Representing equilibrium and nonequilibrium convection in large-scale  
771 models. *Journal of the Atmospheric Sciences*, 71(2), 734-753.  
772 <https://doi.org/10.1175/JAS-D-13-0163.1>, 2014.
- 773 Bryan, G. H., and H. Morrison: Sensitivity of a simulated squall line to horizontal resolution  
774 and parameterization of microphysics. *Mon. Wea. Rev.*, 140, 202–225,  
775 <https://doi.org/10.1175/MWR-D-11-00046.1>, 2012.
- 776 Burakowski, E. A., Tawfik, A., Ouimette, A., Lepine, L., Zarzycki, C., Novick, K., ... & Bonan,  
777 G.: Simulating surface energy fluxes using the variable-resolution Community Earth  
778 System Model (VR-CESM). *Theoretical and Applied Climatology*, 1-19.  
779 <https://doi.org/10.1007/s00704-019-02785-0>, 2019.
- 780 Chauvin, F., J.-F. Royer, and M. Deque: Response of hurricane type vortices to global warming  
781 as simulated by ARPEGE-Climat at high resolution. *Climate Dyn.*, 27, 377-399,  
782 <https://doi.org/10.1007/s00382-006-0135-7>, 2006.
- 783 Chen, F., & Dudhia, J.: Coupling an advanced land surface–hydrology model with the Penn  
784 State–NCAR MM5 modeling system. Part I: Model implementation and

785 sensitivity. *Monthly Weather Review*, 129(4), 569-585. [https://doi.org/10.1175/1520-0493\(2001\)129<0569:CAALSH>2.0.CO;2](https://doi.org/10.1175/1520-0493(2001)129<0569:CAALSH>2.0.CO;2), 2001.

786

787 Déqué, M., Jones, R. G., Wild, M., Giorgi, F., Christensen, J. H., Hassell, D. C., ... & De Castro, M.: Global high resolution versus Limited Area Model climate change projections over Europe: quantifying confidence level from PRUDENCE results. *Climate Dynamics*, 25(6), 653-670. <https://doi.org/10.1007/s00382-005-0052-1>, 2005.

788

789

790

791 Déqué, M., & Piedelievre, J. P.: High resolution climate simulation over Europe. *Climate dynamics*, 11(6), 321-339. <https://doi.org/10.1007/BF00215735>, 1995.

792

793 Déqué, M., Rowell, D. P., Lüthi, D., Giorgi, F., Christensen, J. H., Rockel, B., ... & van den Hurk, B. J. J. M.: An intercomparison of regional climate simulations for Europe: assessing uncertainties in model projections. *Climatic Change*, 81(1), 53-70. <https://doi.org/10.1007/s10584-006-9228-x>, 2007.

794

795

796

797 Ding, Y., Wang, Z., & Sun, Y.: Inter-decadal variation of the summer precipitation in East China and its association with decreasing Asian summer monsoon. Part I: Observed evidences. *International Journal of Climatology*, 28(9), 1139-1161. <https://doi.org/10.1002/joc.1615>, 2008.

798

799

800

801 Clark, P., Roberts, N., Lean, H., Ballard, S. P., & Charlton-Perez, C.: Convection-permitting models: a step-change in rainfall forecasting. *Meteorological Applications*, 23(2), 165-181. <https://doi.org/10.1002/met.1538>, 2016.

802

803

804 Du, Q., Faber, V., & Gunzburger, M.: Centroidal Voronoi tessellations: Applications and algorithms. *SIAM review*, 41(4), 637-676. <https://doi.org/10.1137/S0036144599352836>, 1999.

805

806

807 ECMWF: ECMWF strategy 2016–2025: The strength of a common goal. European Centre for Medium-Range Weather Forecasts Tech. Rep., 32 pp. [https://www.ecmwf.int/sites/default/files/ECMWF\\_Strategy\\_2016-2025.pdf](https://www.ecmwf.int/sites/default/files/ECMWF_Strategy_2016-2025.pdf), 2016.

808

809

810 Efron, B.: Bootstrap methods: another look at the jackknife. In *Breakthroughs in statistics* (pp. 569-593). Springer, New York, NY. [https://doi.org/10.1007/978-1-4612-4380-9\\_41](https://doi.org/10.1007/978-1-4612-4380-9_41), 1992.

811

812

813 Efron, B., & Tibshirani, R. J.: *An introduction to the bootstrap*. CRC press, 1994.

814 Fan, J., Rosenfeld, D., Yang, Y., Zhao, C., Leung, L. R., & Li, Z.: Substantial contribution of anthropogenic air pollution to catastrophic floods in Southwest China. *Geophysical Research Letters*, 42(14), 6066-6075. <https://doi.org/10.1002/2015GL064479>, 2015.

815

816

817 Feng, Z., L.R. Leung, R.A. Houze, Jr., S. Hagos, J. Hardin, Q. Yang, B. Han, & J. Fan:  
818 Structure and evolution of mesoscale convective systems: sensitivity to cloud  
819 microphysics in convection-permitting simulations over the U.S. *J. Adv. Model. Earth*  
820 *Syst.*, 10, <https://doi.org/10.1029/2018MS001305>, 2018.

821 Fowler, L. D., Skamarock, W. C., Grell, G. A., Freitas, S. R., & Duda, M. G.: Analyzing the  
822 Grell–Freitas convection scheme from hydrostatic to nonhydrostatic scales within a  
823 global model. *Monthly Weather Review*, 144(6), 2285-2306.  
824 <https://doi.org/10.1175/MWR-D-15-0311.1>, 2016.

825 Fritsch, J. M., & Carbone, R. E.: Improving quantitative precipitation forecasts in the warm  
826 season: A USWRP research and development strategy. *Bulletin of the American*  
827 *Meteorological Society*, 85(7), 955-966. <https://doi.org/10.1175/BAMS-85-7-955>,  
828 2004.

829 Gao, Y., L.R. Leung, C. Zhao, & S. Hagos: Sensitivity of summer precipitation to model  
830 resolution and convective parameterizations across gray zone resolutions. *J. Geophys.*  
831 *Res.*, 122, 2714-2733, doi:10.1002/2016JD025896, 2017.

832 Gettelman, A., Callaghan, P., Larson, V. E., Zarzycki, C. M., Bacmeister, J. T., Lauritzen, P.  
833 H., ... & Neale, R. B.: Regional climate simulations with the community earth system  
834 model. *Journal of Advances in Modeling Earth Systems*, 10(6), 1245-1265.  
835 <https://doi.org/10.1002/2017MS001227>, 2018.

836 Gettelman A., Morrison H., Thompson G.: Cloud Microphysics Across Scales for Weather and  
837 Climate. In: Randall D., Srinivasan J., Nanjundiah R., Mukhopadhyay P. (eds) *Current*  
838 *Trends in the Representation of Physical Processes in Weather and Climate Models.*  
839 Springer Atmospheric Sciences. Springer, Singapore, 2019.

840 Giorgi, F., and Marinucci, M. R.: A investigation of the sensitivity of simulated precipitation  
841 to model resolution and its implications for climate studies. *Monthly Weather*  
842 *Review*, 124(1), 148-166. [https://doi.org/10.1175/1520-](https://doi.org/10.1175/1520-0493(1996)124<0148:AIOTSO>2.0.CO;2)  
843 [0493\(1996\)124<0148:AIOTSO>2.0.CO;2](https://doi.org/10.1175/1520-0493(1996)124<0148:AIOTSO>2.0.CO;2), 1996.

844 Giorgi, F., and Mearns, L. O.: Approaches to the simulation of regional climate change: a  
845 review. *Reviews of Geophysics*, 29(2), 191-216. <https://doi.org/10.1029/90RG02636>,  
846 1991.

847 Grell, G. A., & Dévényi, D.: A generalized approach to parameterizing convection combining  
848 ensemble and data assimilation techniques. *Geophysical Research Letters*, 29(14), 38-  
849 1. <https://doi.org/10.1029/2002GL015311>, 2002.

850 Grell, G. A., & Freitas, S. R.: A scale and aerosol aware stochastic convective parameterization  
851 for weather and air quality modeling. *Atmos. Chem. Phys*, 14(10), 5233-5250.  
852 <https://doi.org/10.5194/acp-14-5233-2014>, 2014.

853 Gross, M., Wan, H., Rasch, P. J., Caldwell, P. M., Williamson, D. L., Klocke, D., Christiane,  
854 J, Diana, T., Nigel, W., Mike, C, Bob, B., Martin, W., Florian, L., Eric, B., Sylvie, M.,  
855 Piet, T., Almut, G., Peter, L., Hans, J., Colin, Z., Sakaguchi, K., Leung, R.: Physics–  
856 Dynamics Coupling in Weather, Climate, and Earth System Models: Challenges and  
857 Recent Progress. *Monthly Weather Review*, 146(11), 3505-3544.  
858 <https://doi.org/10.1175/MWR-D-17-0345.1>, 2018.

859 Guo, J., Su, T., Li, Z., Miao, Y., Li, J., Liu, H., Xu, H., Cribb, M., and Zhai, P.: Declining  
860 frequency of summertime local-scale precipitation over eastern China from 1970 to  
861 2010 and its potential link to aerosols. *Geophysical Research Letters*, 44(11), 5700-  
862 5708, 2017.

863 Hagos, S., Leung, L. R., Yang, Q., Zhao, C., and Lu, J.: Resolution and dynamical core  
864 dependence of atmospheric river frequency in global model simulations. *Journal of*  
865 *Climate*, 28(7), 2764-2776. <https://doi.org/10.1175/JCLI-D-14-00567.1>, 2015.

866 Herrington, A. R., & Reed, K. A.: An explanation for the sensitivity of the mean state of the  
867 community atmosphere model to horizontal resolution on aquaplanets. *Journal of*  
868 *Climate*, 30(13), 4781-4797. <https://doi.org/10.1175/JCLI-D-16-0069.1>, 2017.

869 Herrington, A. R., & Reed, K. A.: An Idealized Test of the Response of the Community  
870 Atmosphere Model to Near - Grid - Scale Forcing Across Hydrostatic  
871 Resolutions. *Journal of Advances in Modeling Earth Systems*, 10(2), 560-575.  
872 <https://doi.org/10.1002/2017MS001078>, 2018.

873 Fildier, B., Parishani, H., & Collins, W. D.: Prognostic Power of Extreme Rainfall Scaling  
874 Formulas Across Space and Time Scales. *Journal of Advances in Modeling Earth*  
875 *Systems*, 10(12), 3252-3267. <https://doi.org/10.1029/2018MS001462>, 2018.

876 Hong, S. Y.: A new stable boundary-layer mixing scheme and its impact on the simulated East  
877 Asian summer monsoon. *Quarterly Journal of the Royal Meteorological*  
878 *Society*, 136(651), 1481-1496. <https://doi.org/10.1002/qj.665>, 2010.

879 Hong, S. Y., & Lim, J. O. J.: The WRF single-moment 6-class microphysics scheme  
880 (WSM6). *J. Korean Meteor. Soc*, 42(2), 129-151, 2006.

881 Hong, S. Y., Noh, Y., & Dudhia, J.: A new vertical diffusion package with an explicit treatment  
882 of entrainment processes. *Monthly weather review*, 134(9), 2318-2341.  
883 <https://doi.org/10.1175/MWR3199.1>, 2006.

884 Huang, X., Rhoades, A. M., Ullrich, P. A., & Zarzycki, C. M.: An evaluation of the variable-  
885 resolution CESM for modeling California's climate. *Journal of Advances in Modeling  
886 Earth Systems*, 8(1), 345-369. <https://doi.org/10.1002/2015MS000559>, 2016.

887 Hui, P., Tang, J., Wang, S., & Wu, J.: Sensitivity of simulated extreme precipitation and  
888 temperature to convective parameterization using RegCM3 in China. *Theoretical and  
889 applied climatology*, 122(1-2), 315-335. <https://doi.org/10.1007/s00704-014-1300-2>,  
890 2015.

891 Iacono, M. J., Mlawer, E. J., Clough, S. A., & Morcrette, J. J.: Impact of an improved longwave  
892 radiation model, RRTM, on the energy budget and thermodynamic properties of the  
893 NCAR community climate model, CCM3. *Journal of Geophysical Research:  
894 Atmospheres*, 105(D11), 14873-14890. <https://doi.org/10.1029/2000JD900091>, 2000.

895 Jeevanjee, N.: Vertical velocity in the gray zone. *Journal of Advances in Modeling Earth  
896 Systems*, 9(6), 2304-2316. <https://doi.org/10.1002/2017MS001059>, 2017.

897 Judt, F.: Insights into Atmospheric Predictability through Global Convection-Permitting Model  
898 Simulations. *Journal of the Atmospheric Sciences*, 75(5), 1477-1497.  
899 <https://doi.org/10.1175/JAS-D-17-0343.1>, 2018.

900 Ju, L., Ringler, T., & Gunzburger, M.: Voronoi tessellations and their application to climate  
901 and global modeling. In *Numerical techniques for global atmospheric models* (pp. 313-  
902 342). Springer, Berlin, Heidelberg. [https://doi.org/10.1007/978-3-642-11640-7\\_10](https://doi.org/10.1007/978-3-642-11640-7_10),  
903 [2011](https://doi.org/10.1007/978-3-642-11640-7_10).

904 Kain, J. S.: The Kain–Fritsch convective parameterization: an update. *Journal of applied  
905 meteorology*, 43(1), 170-181. [https://doi.org/10.1175/1520-  
906 0450\(2004\)043<0170:TKCPAU>2.0.CO;2](https://doi.org/10.1175/1520-0450(2004)043<0170:TKCPAU>2.0.CO;2), 2004.

907 Kain, J. S., Weiss, S. J., Bright, D. R., Baldwin, M. E., Levit, J. J., Carbin, G. W., ... & Thomas,  
908 K. W.: Some practical considerations regarding horizontal resolution in the first  
909 generation of operational convection-allowing NWP. *Weather and Forecasting*, 23(5),  
910 931-952. <https://doi.org/10.1175/WAF2007106.1>, 2008.

911 Klemp, J. B.: A terrain-following coordinate with smoothed coordinate surfaces. *Monthly  
912 weather review*, 139(7), 2163-2169. <https://doi.org/10.1175/MWR-D-10-05046.1>,  
913 2011.

914 Klemp, J. B., Skamarock, W. C., & Dudhia, J.: Conservative split-explicit time integration  
915 methods for the compressible nonhydrostatic equations. *Monthly Weather*  
916 *Review*, 135(8), 2897-2913. <https://doi.org/10.1175/MWR3440.1>, 2007.

917 Landu, K., Leung, L. R., Hagos, S., Vinoj, V., Rauscher, S. A., Ringler, T., & Taylor, M.: The  
918 dependence of ITCZ structure on model resolution and dynamical core in aquaplanet  
919 simulations. *Journal of Climate*, 27(6), 2375-2385. [https://doi.org/10.1175/JCLI-D-13-](https://doi.org/10.1175/JCLI-D-13-00269.1)  
920 00269.1, 2014.

921 Laprise, R.: Regional climate modelling. *Journal of Computational Physics*, 227(7), 3641-3666.  
922 <https://doi.org/10.1016/j.jcp.2006.10.024>, 2008.

923 Leung, L. R., & Qian, Y.: The sensitivity of precipitation and snowpack simulations to model  
924 resolution via nesting in regions of complex terrain. *Journal of Hydrometeorology*, 4(6),  
925 1025-1043. [https://doi.org/10.1175/1525-7541\(2003\)004<1025:TSOPAS>2.0.CO;2](https://doi.org/10.1175/1525-7541(2003)004<1025:TSOPAS>2.0.CO;2),  
926 2003.

927 Leung, L. R., Ringler, T., Collins, W. D., Taylor, M., & Ashfaq, M.: A hierarchical evaluation  
928 of regional climate simulations. *Eos, Transactions American Geophysical*  
929 *Union*, 94(34), 297-298. <https://doi.org/10.1002/2013EO340001>, 2013.

930 Li, J., Zhang, Q., Chen, Y. D., & Singh, V. P.: GCM simulations. *Eos, Transactions American*  
931 *Ge extremes during the 21st century in China. Journal of Geophysical Research:*  
932 *Atmospheres*, 118(19). <https://doi.org/10.1002/jgrd.50851>, 2013.

933 Li, W., Jiang, Z., Xu, J., & Li, L.: Extreme Precipitation Indices over China in CMIP5 Models.  
934 Part II: Probabilistic Projection. *Journal of Climate*, 29(24), 8989-9004.  
935 <https://doi.org/10.1175/JCLI-D-16-0377.1>, 2016.

936 Li, Z., W. K.-M. Lau, V. Ramanathan et al.: Aerosol and monsoon climate interactions over  
937 Asia, *Rev. Geophys.*, 54, <https://doi.org/10.1002/2015RG000500>, 2016.

938 Lin, Z., & Wang, B.: Northern East Asian low and its impact on the interannual variation of  
939 East Asian summer rainfall. *Climate dynamics*, 46(1-2), 83-97.  
940 <https://doi.org/10.1007/s00382-015-2570-9>, 2016.

941 Liu, R., Liu, S. C., Cicerone, R. J., Shiu, C. J., Li, J., Wang, J., & Zhang, Y.: Trends of extreme  
942 precipitation in eastern China and their possible causes. *Advances in Atmospheric*  
943 *Sciences*, 32(8), 1027-1037. <https://doi.org/10.1007/s00376-015-5002->, 2015.

944 Locatelli, J. D., & Hobbs, P. V.: Fall speeds and masses of solid precipitation particles. *Journal*  
945 *of Geophysical Research*, 79(15), 2185-2197.  
946 <https://doi.org/10.1029/JC079i015p02185>, 1974.

947 Lorant, V., & Royer, J. F.: Sensitivity of equatorial convection to horizontal resolution in  
948 aquaplanet simulations with a variable-resolution GCM. *Monthly weather*  
949 *review*, 129(11), 2730-2745. [https://doi.org/10.1175/1520-](https://doi.org/10.1175/1520-0493(2001)129<2730:SOECTH>2.0.CO;2)  
950 [0493\(2001\)129<2730:SOECTH>2.0.CO;2](https://doi.org/10.1175/1520-0493(2001)129<2730:SOECTH>2.0.CO;2), 2001.

951 Lu, J., Chen, G., Leung, L. R., Burrows, D. A., Yang, Q., Sakaguchi, K., & Hagos, S.: Toward  
952 the dynamical convergence on the jet stream in aquaplanet AGCMs. *Journal of*  
953 *Climate*, 28(17), 6763-6782. <https://doi.org/10.1175/JCLI-D-14-00761.1>, 2015.

954 Mlawer, E. J., Taubman, S. J., Brown, P. D., Iacono, M. J., & Clough, S. A.: Radiative transfer  
955 for inhomogeneous atmospheres: RRTM, a validated correlated -k model for the  
956 longwave. *Journal of Geophysical Research: Atmospheres*, 102(D14), 16663-16682.  
957 <https://doi.org/10.1029/97JD00237.>, 1997.

958 Molthan, A. L., & Colle, B. A.: Comparisons of single-and double-moment microphysics  
959 schemes in the simulation of a synoptic-scale snowfall event. *Monthly Weather Review*,  
960 140(9), 2982-3002. <https://doi.org/10.1175/MWR-D-11-00292.1>, 2012.

961 Nakanishi, M., & Niino, H.: An improved Mellor–Yamada level-3 model: Its numerical  
962 stability and application to a regional prediction of advection fog. *Boundary-Layer*  
963 *Meteorology*, 119(2), 397-407. <https://doi.org/10.1007/s10546-005-9030-8>, 2006.

964 Nakanishi, M., & Niino, H.: Development of an improved turbulence closure model for the  
965 atmospheric boundary layer. *Journal of the Meteorological Society of Japan. Ser.*  
966 *II*, 87(5), 895-912. <https://doi.org/10.2151/jmsj.87.895>, 2009.

967 NRC: National Research Council Board, *A National Strategy for Advancing Climate Modeli*  
968 *ng*, The National Academies Press, Washington, DC (2012) ([http://www.nap.edu/cata](http://www.nap.edu/catalog/13430/a-national-strategy-for-advancing-climate-modeling)  
969 [log/13430/a-national-strategy-for-advancing-climate-](http://www.nap.edu/catalog/13430/a-national-strategy-for-advancing-climate-modeling)  
970 [modeling](http://www.nap.edu/catalog/13430/a-national-strategy-for-advancing-climate-modeling), last access: April 25, 2019).

971 O'Brien, T. A., Collins, W. D., Kashinath, K., Rübél, O., Byna, S., Gu, J., Krishnan, H, Ullrich,  
972 P.: Resolution dependence of precipitation statistical fidelity in hindcast  
973 simulations. *Journal of Advances in Modeling Earth Systems*, 8(2), 976-990.  
974 <https://doi.org/10.1002/2016MS000671>, 2016.

975 O'Brien, T. A., Li, F., Collins, W. D., Rauscher, S. A., Ringler, T. D., Taylor, M., Hagos, S.  
976 M., Leung, L. R.: Observed scaling in clouds and precipitation and scale incognizance  
977 in regional to global atmospheric models. *Journal of Climate*, 26(23), 9313-9333.  
978 <https://doi.org/10.1175/JCLI-D-13-00005.1>, 2013.

979 Park, S. H., Skamarock, W. C., Klemp, J. B., Fowler, L. D., & Duda, M. G.: Evaluation of  
980 global atmospheric solvers using extensions of the Jablonowski and Williamson  
981 baroclinic wave test case. *Monthly Weather Review*, 141(9), 3116-3129.  
982 <https://doi.org/10.1175/MWR-D-12-00096.1>, 2013.

983 Pedersen, C. A., & Winther, J. G.: Intercomparison and validation of snow albedo  
984 parameterization schemes in climate models. *Climate Dynamics*, 25(4), 351-362:  
985 <https://doi.org/10.1007/s00382-005-0037-0>, 2005.

986 Prein, A. F., Langhans, W., Fosser, G., Ferrone, A., Ban, N., Goergen, K., ... & Brisson, E.: A  
987 review on regional convection - permitting climate modeling: Demonstrations,  
988 prospects, and challenges. *Reviews of geophysics*, 53(2), 323-361.  
989 <https://doi.org/10.1002/2014RG000475>, 2015.

990 Prein, A. F., Rasmussen, R. M., Ikeda, K., Liu, C., Clark, M. P., & Holland, G. J.: The future  
991 intensification of hourly precipitation extremes. *Nature Climate Change*, 7(1), 48.  
992 <https://doi.org/10.1038/nclimate3168>, 2017.

993 Rauscher, S. A., O'Brien, T. A., Piani, C., Coppola, E., Giorgi, F., Collins, W. D., & Lawston,  
994 P. M.: A multimodel intercomparison of resolution effects on precipitation: simulations  
995 and theory. *Climate dynamics*, 47(7-8), 2205-2218. <https://doi.org/10.1007/s00382-015-2959-5>, 2016.

997 Rauscher, S. A., Ringler, T. D., Skamarock, W. C., & Mirin, A. A.: Exploring a global  
998 multiresolution modeling approach using aquaplanet simulations. *Journal of  
999 Climate*, 26(8), 2432-2452. <https://doi.org/10.1175/JCLI-D-12-00154.1>, 2013.

1000 Rhoades, A. M., Huang, X., Ullrich, P. A., & Zarzycki, C. M.: Characterizing Sierra Nevada  
1001 snowpack using variable-resolution CESM. *Journal of Applied Meteorology and  
1002 Climatology*, 55(1), 173-196. <https://doi.org/10.1175/JAMC-D-15-0156.1>, 2016.

1003 Rhoades, A. M., Ullrich, P. A., Zarzycki, C. M., Johansen, H., Margulis, S. A., Morrison, H., ...  
1004 & Collins, W. D.: Sensitivity of Mountain Hydroclimate Simulations in Variable-  
1005 Resolution CESM to Microphysics and Horizontal Resolution. *Journal of Advances in  
1006 Modeling Earth Systems*, 10(6), 1357-1380. <https://doi.org/10.1029/2018MS001326>,  
1007 2018.

1008 Ringler, T. D., Jacobsen, D., Gunzburger, M., Ju, L., Duda, M., & Skamarock, W.: Exploring  
1009 a multiresolution modeling approach within the shallow-water equations. *Monthly  
1010 Weather Review*, 139(11), 3348-3368. <https://doi.org/10.1175/MWR-D-10-05049.1>,  
1011 2011.

1012 Ringler, T., Ju, L., & Gunzburger, M.: A multiresolution method for climate system modeling:  
 1013 Application of spherical centroidal Voronoi tessellations. *Ocean Dynamics*, 58(5-6),  
 1014 475-498. <https://doi.org/10.1007/s10236-008-0157-2>, 2008.

1015 Sakaguchi, K., Leung, L. R., Zhao, C., Yang, Q., Lu, J., Hagos, S.: Exploring a multiresolution  
 1016 approach using AMIP simulations. *Journal of Climate*, 28(14), 5549-5574.  
 1017 <https://doi.org/10.1175/JCLI-D-14-00729.1>, 2015.

1018 Sakaguchi, K., Lu, J., Leung, L. R., Zhao, C., Li, Y., & Hagos, S.: Sources and pathways of  
 1019 the upscale effects on the Southern Hemisphere jet in  
 1020 MPASs. s. ions. s. ons. ultiresolution approach using AMIP simulations. *nd*  
 1021 Williams25-10431043 4(6<https://doi.org/10.1002/2016MS000743>, 2016.

1022 Skamarock, W. C., & Gassmann, A.: Conservative transport schemes for spherical geodesic  
 1023 grids: High-order flux operators for ODE-based time integration. *Monthly Weather*  
 1024 *Review*, 139(9), 2962-2975. <https://doi.org/10.1175/MWR-D-10-05056.1>, 2011.

1025 Skamarock, W. C., & Klemp, J. B.: A time-split nonhydrostatic atmospheric model for weather  
 1026 research and forecasting applications. *Journal of Computational Physics*, 227(7), 3465-  
 1027 3485. <https://doi.org/10.1016/j.jcp.2007.01.037>, 2008.

1028 Skamarock, W. C., Klemp, J. B., Duda, M. G., Fowler, L. D., Park, S. H., & Ringler, T. D.: A  
 1029 multiscale nonhydrostatic atmospheric model using centroidal Voronoi tessellations and  
 1030 C-grid staggering. *Monthly Weather Review*, 140(9), 3090-3105.  
 1031 <https://doi.org/10.1175/MWR-D-11-00215.1>, 2012.

1032 Sukovich, E. M., Ralph, F. M., Barthold, F. E., Reynolds, D. W., & Novak, D. R.: Extreme  
 1033 quantitative precipitation forecast performance at the Weather Prediction Center from  
 1034 2001 to 2011. *Weather and Forecasting*, 29(4), 894-911. [https://doi.org/10.1175/WAF-](https://doi.org/10.1175/WAF-D-13-00061.1)  
 1035 [D-13-00061.1](https://doi.org/10.1175/WAF-D-13-00061.1), 2014.

1036 Thompson, G., Field, P. R., Rasmussen, R. M., & Hall, W. D.: Explicit forecasts of winter  
 1037 precipitation using an improved bulk microphysics scheme. Part II: Implementation of  
 1038 a new snow parameterization. *Monthly Weather Review*, 136(12), 5095-5115.  
 1039 <https://doi.org/10.1175/2008MWR2387.1>, 2008.

1040 Wang, M., & Ullrich, P.: Marine air penetration in California's Central Valley: Meteorological  
 1041 drivers and the impact of climate change. *Journal of Applied Meteorology and*  
 1042 *Climatology*, 57(1), 137-154. <https://doi.org/10.1175/JAMC-D-17-0089.1>, 2018.

1043 Wang, Y., Leung, L. R., McGREGOR, J. L., Lee, D. K., Wang, W. C., Ding, Y., & Kimura,  
 1044 F.: Regional climate modeling: progress, challenges, and prospects. *Journal of the*

- 1045 Meteorological Society of Japan. Ser. II, 82(6), 1599-1628.  
1046 <https://doi.org/10.2151/jmsj.82.1599>, 2004.
- 1047 Wicker, L. J., & Skamarock, W. C.: Time-splitting methods for elastic models using forward  
1048 time schemes. *Monthly weather review*, 130(8), 2088-2097.  
1049 [https://doi.org/10.1175/1520-0493\(2002\)130<2088:TSMFEM>2.0.CO;2](https://doi.org/10.1175/1520-0493(2002)130<2088:TSMFEM>2.0.CO;2), 2002.
- 1050 Wu, C., Liu, X., Lin, Z., Rhoades, A. M., Ullrich, P. A., Zarzycki, C. M., ... & Rahimi-Esfarjani,  
1051 S. R.: Exploring a variable-resolution approach for simulating regional climate in the  
1052 Rocky Mountain region using the VR-CESM. *Journal of Geophysical Research:*  
1053 *Atmospheres*, 122(20), 10-939. <https://doi.org/10.1002/2017JD027008>, 2017.
- 1054 Xiang, S., Li, Y., Li, D., & Yang, S.: An analysis of heavy precipitation caused by a retracing  
1055 plateau vortex based on TRMM data. *Meteorology and Atmospheric Physics*, 122(1-2),  
1056 33-45. <https://doi.org/10.1007/s00703-013-0269-1>, 2013.
- 1057 Xu, H., & Yao, W.: A numerical study of the Beijing extreme rainfall of 21 July 2012 and the  
1058 impact of topography. *Advances in Meteorology*, 2015.  
1059 <http://dx.doi.org/10.1155/2015/980747>, 2015.
- 1060 Xue, M., Kong, F., Weber, D., Thomas, K. W., Wang, Y., Brewster, K., ... & Coniglio, M. C.:  
1061 CAPS realtime storm-scale ensemble and high-resolution forecasts as part of the  
1062 NOAA Hazardous Weather Testbed 2007 spring experiment. In *22nd Conf. Wea. Anal.*  
1063 *Forecasting/18th Conf. Num. Wea. Pred*, 2007.
- 1064 Xu, Z., Rhoades, A. M., Johansen, H., Ullrich, P. A., & Collins, W. D.: An intercomparison of  
1065 GCM and RCM dynamical downscaling for characterizing the hydroclimatology of  
1066 California and Nevada. *Journal of Hydrometeorology*, 19(9), 1485-1506.  
1067 <https://doi.org/10.1175/JHM-D-17-0181.1>, 2018.
- 1068 Yang, Q., Leung, L. R., Rauscher, S. A., Ringler, T. D., & Taylor, M. A.: Atmospheric moisture  
1069 budget and spatial resolution dependence of precipitation extremes in aquaplanet  
1070 simulations. *Journal of Climate*, 27(10), 3565-3581. [https://doi.org/10.1175/JCLI-D-](https://doi.org/10.1175/JCLI-D-13-00468.1)  
1071 [13-00468.1](https://doi.org/10.1175/JCLI-D-13-00468.1), 2014.
- 1072 Yang, Q., R. Houze, Jr., L.R. Leung, & Z. Feng : Environments of long-lived mesoscale  
1073 convective systems over the Central United States in convection permitting climate  
1074 simulations. *J. Geophys. Res.*, 122, <https://doi.org/10.1002/2017JD027033>, 2017.
- 1075 Yao, X. P., Sun, J. Y., & Ma J. L.: Advances on research of Yangtze-Huaihe shear line. *Plateau*  
1076 *Meteorology*, 36(4), 1138-1151 (in Chinese), 2017.

1077 Yessad, K., & Bénard, P.: Introduction of a local mapping factor in the spectral part of the  
1078 Météo-France global variable mesh numerical forecast model. Quarterly Journal of the  
1079 Royal Meteorological Society, 122(535), 1701-1719.  
1080 <https://doi.org/10.1002/qj.49712253511>, 1996.

1081 Zarzycki, C. M., Jablonowski, C., & Taylor, M. A.: Using variable resolution meshes to model  
1082 tropical cyclones in the community atmosphere model. Monthly Weather Review,  
1083 142(3), 1221–1239. <https://doi.org/10.1175/MWR-D-13-00179.1>, 2014.

1084 Zarzycki CM, Jablonowski C, Thatcher DR, Taylor MA: Effects of localized grid refinement  
1085 on the general circulation and climatology in the community atmosphere model. J Clim  
1086 28:2777–2803. <https://doi.org/10.1175/JCLI-D-14-00599.1>, 2015.

1087 Zhang, D. L., Lin, Y., Zhao, P., Yu, X., Wang, S., Kang, H., & Ding, Y.: The Beijing extreme  
1088 rainfall of 21 July 2012: “Right results” but for wrong reasons. Geophysical Research  
1089 Letters, 40(7), 1426-1431. <https://doi.org/10.1002/grl.50304>, 2013.

1090 Zhang, H., & Zhai, P.: Temporal and spatial characteristics of extreme hourly precipitation  
1091 over eastern China in the warm season. Advances in atmospheric sciences, 28(5), 1177.  
1092 <https://doi.org/10.1007/s00376-011-0020-0>, 2011.

1093 Zhang, L., Dong, M., & Wu, T.: Changes in precipitation extremes over eastern China  
1094 simulated by the Beijing Climate Center Climate System Model (BCC\_CSM1.  
1095 0). Climate Research, 50(2-3), 227-245. <https://doi.org/10.3354/cr01066>, 2011.

1096 Zhang, Q., Xiao, M., Singh, V. P., Liu, L., & Xu, C. Y.: Observational evidence of summer  
1097 precipitation deficit-temperature coupling in China. Journal of Geophysical Research:  
1098 Atmospheres, 120(19). <https://doi.org/10.1002/2015JD023830>, 2011.

1099 Zhang, Q., Zheng, Y., Singh, V. P., Luo, M., & Xie, Z.: Summer extreme precipitation in  
1100 eastern China: Mechanisms and impacts. Journal of Geophysical Research:  
1101 Atmospheres, 122(5), 2766-2778. <https://doi.org/10.1002/2016JD025913>, 2017.

1102 Zhang, Y., P., L., & Zhong, Q.: An interdecadal change in the relationship between the western  
1103 North Pacific Ocean and the East Asian summer monsoon. Climate Dynamics, 49(4),  
1104 1139-1156. <https://doi.org/10.1007/s00382-016-3370-6>, 2017.

1105 Zhai, P., Zhang, X., Wan, H., & Pan, X.: Trends in total precipitation and frequency of daily  
1106 precipitation extremes over China. Journal of Climate, 18(7), 1096-1108.  
1107 <https://doi.org/10.1175/JCLI-3318.1>, 2005.

1108 Zhao, C., Leung, L. R., Park, S. H., Hagos, S., Lu, J., Sakaguchi, K., ... & Duda, M. G.:  
1109 Exploring the impacts of physics and resolution on aqua, planet simulations from a

1110 nonhydrostatic global variable resolution modeling framework. *Journal of Advances*  
1111 *in Modeling Earth Systems*, 8(4), 1751-1768. <https://doi.org/10.1002/2016MS000727>,  
1112 2017.

1113 Zhao, Y., Xu, X., Zhao, T., Xu, H., Mao, F., Sun, H., & Wang, Y.: Extreme precipitation events  
1114 in East China and associated moisture transport pathways. *Science China Earth*  
1115 *Sciences*, 59(9), 1854-1872. <https://doi.org/10.1007/s11430-016-5315-7>, 2016.

1116 Zheng, Y., Xue, M., Li, B., Chen, J., & Tao, Z.: Spatial characteristics of extreme rainfall over  
1117 China with hourly through 24-hour accumulation periods based on national-level  
1118 hourly rain gauge data. *Advances in Atmospheric Sciences*, 33(11), 1218-1232.  
1119 <https://doi.org/10.1007/s00376-016-6128-5>, 2016.

1120 Zhong, S., Qian, Y., Zhao, C., Leung, R., & Yang, X. Q.: A case study of urbanization impact  
1121 on summer precipitation in the Greater Beijing Metropolitan Area: Urban heat island  
1122 versus aerosol effects. *Journal of Geophysical Research: Atmospheres*, 120(20), 10-  
1123 903. <https://doi.org/10.1002/2015JD023753>, 2015.

1124 Zhong, S., Qian, Y., Zhao, C., Leung, R., Wang, H., Yang, B., ... & Liu, D.: Urbanization-  
1125 induced urban heat island and aerosol effects on climate extremes in the Yangtze River  
1126 Delta region of China. *Atmospheric Chemistry and Physics*, 17(8), 5439-5457.  
1127 <https://doi.org/10.5194/acp-17-5439-2017>, 2017.

1128 Zhou, T. J., & Li, Z.: Simulation of the East Asian summer monsoon using a variable resolution  
1129 atmospheric GCM. *Climate Dynamics*, 19(2), 167-180.  
1130 <https://doi.org/10.1007/s00382-001-0214-8>, 2002.

1131  
1132  
1133

1134

1135

**Table 1** Numerical Experiments conducted and analyzed in this study

Physics/Resolution	MPAS				
	U15km	U60km	V30km	V16km	V4km
WSM6+NTD	Yes	/	/	Yes	/
WSM6+GF	Yes	Yes	Yes	Yes	Yes
Thompson+GF	/	/	/	/	Yes

1136

1137 (1) ‘U’ and ‘V’ represent quasi-uniform and variable resolution meshes, respectively, as  
 1138 described in the Section 2.1.2.

1139 (2) ‘WSM6’ and ‘Thompson’ represent two cloud microphysics schemes as described in the  
 1140 Section 2.1.1; ‘NTD’ and ‘GF’ represent two cumulus parameterizations as described in the  
 1141 Section 2.1.1.

1142

1143 **Table 2** The mean bias (MB) and root mean square root (RMSE) of the simulated results shown  
 1144 in Fig. 6-8, 10 against CMA observations

	GFS.1deg		GFS.0.5deg		U60km.WSM6		V30km.WSM6		V16km.WSM6		V4km.WSM6		V4km.Thompson	
	RMSE	MB	RMSE	MB	RMSE	MB	RMSE	MB	RMSE	MB	RMSE	MB	RMSE	MB
Fig.6 [mm/day]	18.48	1.08	19.62	1.65	14.98	1.99	18.83	5.11	16.80	3.81	14.17	0.59	17.57	3.70
Fig.7 [mm/day]	18.10	0.70	18.79	1.73	9.67	2.18	10.10	3.70	6.31	2.56	3.34	0.31	13.61	5.50
Fig.8 [mm/hour]	1.17	0.06	1.21	0.10	0.78	0.12	0.86	0.18	0.74	0.14	0.83	0.04	1.22	0.26
Fig.10 [mm/day]	/	/	/	/	21.98	-0.49	28.13	7.43	24.27	3.74	21.25	2.28	25.66	6.48

1145

1146

1147 **Table 3** The correlation coefficients and the corresponding 95% confidence intervals based  
 1148 on the bootstrap analysis for the results shown in Fig. 6-10

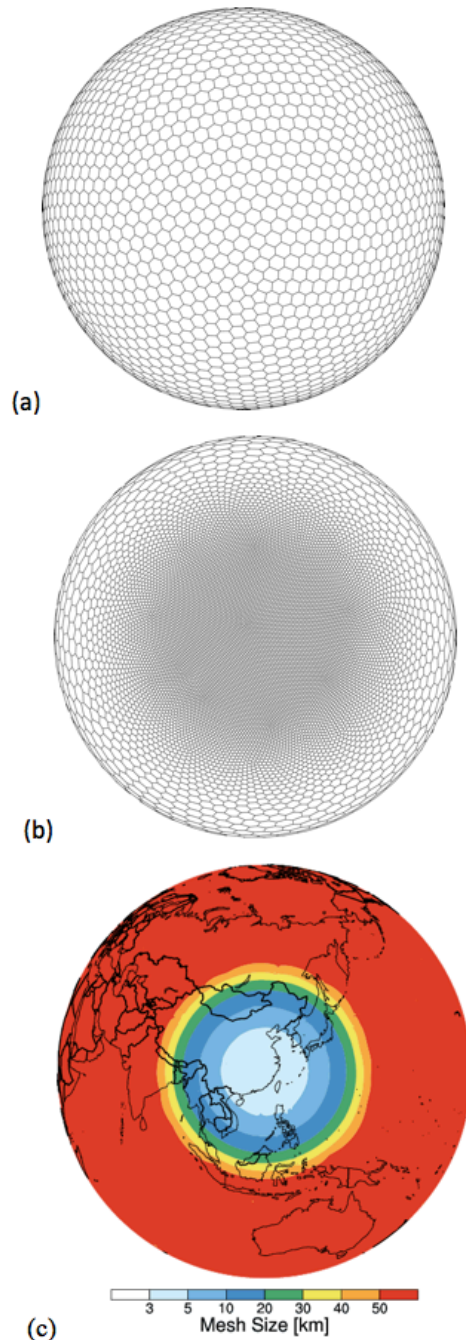
	GFS.1deg	GFS.0.5deg	U60km.WSM6	V30km.WSM6	V16km.WSM6	V4km.WSM6	V4km.Thompson
Fig. 6	0.06 (0.006~0.1)	0.03 (-0.01~0.08)	0.49 (0.45~0.54)	0.47 (0.43~0.53)	0.56 (0.50~0.61)	0.63 (0.54~0.67)	0.54 (0.48~0.59)
Fig. 7	-0.15 (-0.35~0.24)	-0.19 (-0.39~0.15)	0.68 (0.49~0.84)	0.71 (0.46~0.88)	0.89 (0.78~0.95)	0.97 (0.93~0.99)	0.72 (0.45~0.93)
Fig. 8	0.03 (-0.02~0.09)	0.02 (-0.03~0.08)	0.30 (0.25~0.37)	0.32 (0.27~0.41)	0.41 (0.37~0.48)	0.42 (0.39~0.49)	0.38 (0.32~0.44)
Fig. 9	0.32 (0.23~0.41)	0.29 (0.20~0.41)	0.53 (0.45~0.61)	0.68 (0.64~0.72)	0.80 (0.77~0.83)	0.85 (0.82~0.88)	0.80 (0.75~0.84)
Fig. 10	/	/	0.20 (0.13~0.28)	0.21 (0.12~0.30)	0.30 (0.19~0.40)	0.50 (0.39~0.59)	0.42 (0.34~0.51)

1149 (1) The values inside the parenthesis indicate the lower and higher bounds of 95% confidence  
 1150 intervals; the values outside are estimated directly based on the results shown in Fig. 6-10.

1151

1152

1153



1154

1155

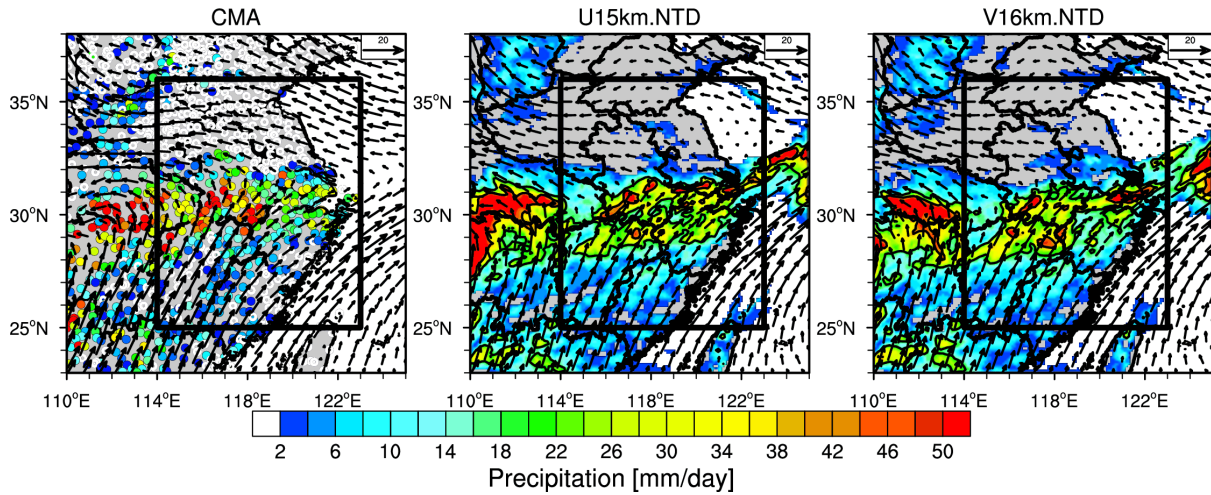
1156 **Figure 1** (a) quasi-uniform mesh and (b) variable-resolution mesh used in the MPAS  
 1157 experiments. Both meshes are plotted at resolutions significantly lower than used in the  
 1158 experiments to show the mesh cells. (c) global variable-resolution mesh size distribution in the  
 1159 variable resolution 4-60 km experiment.

1160

1161

1162

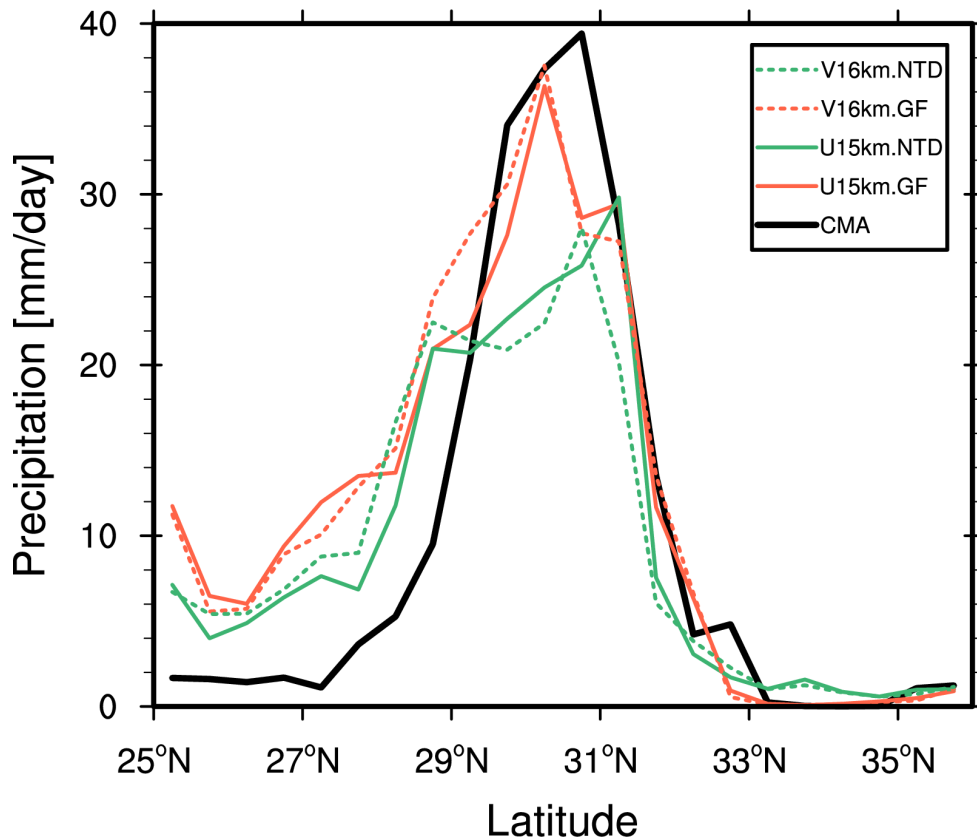
1163  
1164  
1165  
1166



1167  
1168  
1169  
1170  
1171  
1172  
1173  
1174  
1175  
1176  
1177  
1178  
1179  
1180  
1181  
1182  
1183  
1184  
1185  
1186  
1187

**Figure 2** Spatial distributions of precipitation and wind fields at 850 hPa averaged during the event (June 25 00:00 to June 27 12:00 UTC time) from the simulations with the global uniform (15 km) and variable (16 km over the refined region as shown in Fig. 1c) resolutions. The observed mean precipitation from the CMA stations and the wind fields from the ERA5 reanalysis are shown. The black contour lines represent the precipitation larger than 20 mm/day. The black box denotes the region of East China (25°N-36°N, 114°E-123°E) for the analysis in the following.

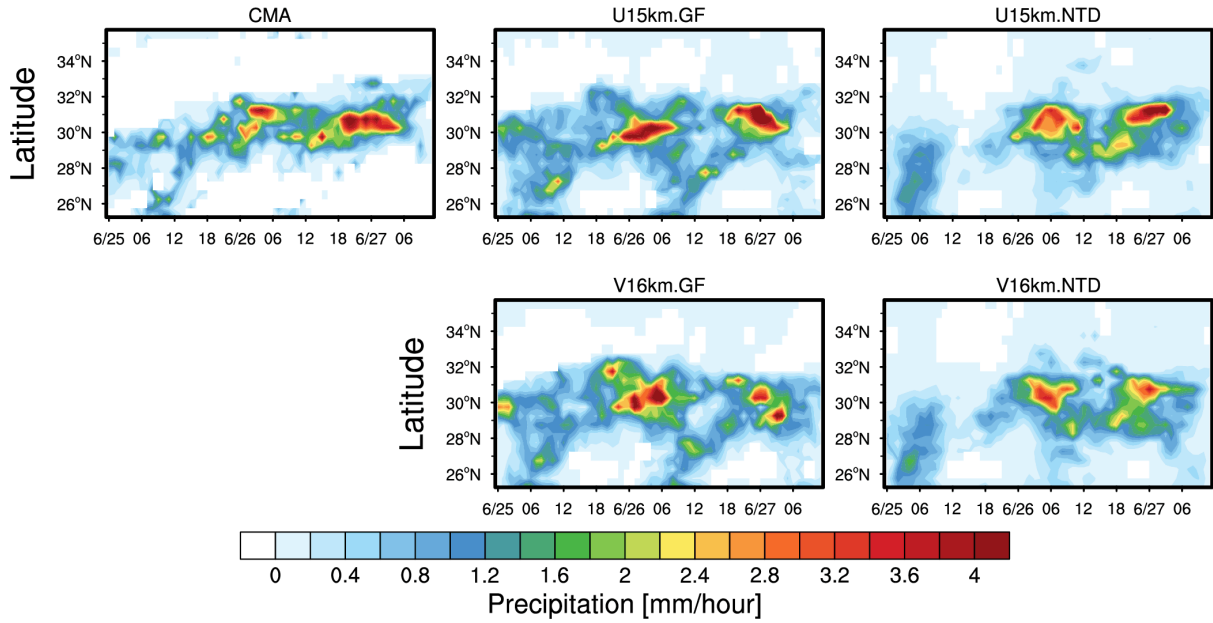
1188  
1189  
1190  
1191  
1192  
1193



1194  
1195  
1196  
1197  
1198  
1199  
1200  
1201  
1202  
1203  
1204  
1205  
1206

**Figure 3** Zonal distributions of precipitation averaged during the event (June 25 00:00 to June 27 12:00 UTC time) averaged over East China (denoted as the black box in Fig. 2) from the CMA station observations and the simulations with the global uniform (15 km, solid lines) and variable (16 km over the refined region as shown in Fig. 1c, dash lines) resolutions with two convective parameterizations (GF, red lines; NTD, green lines). The modeling results are sampled at the CMA station.

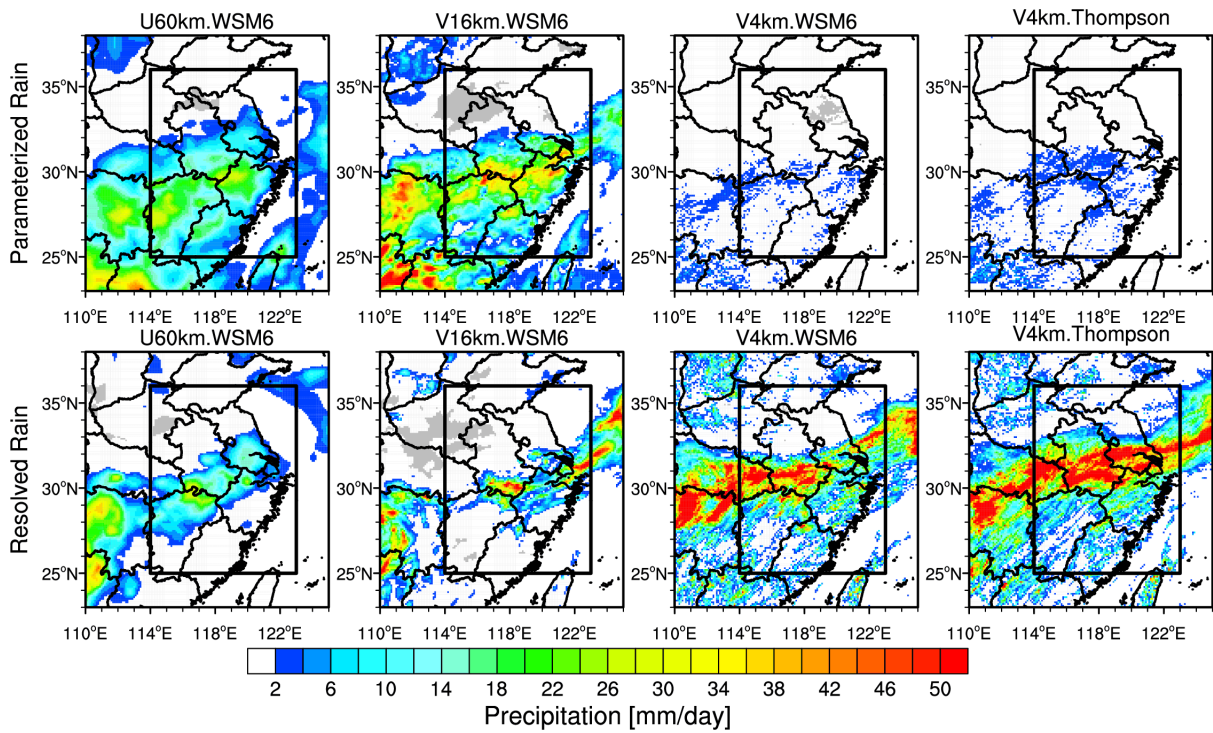
1207  
1208  
1209  
1210  
1211  
1212  
1213



1214  
1215  
1216  
1217  
1218  
1219  
1220  
1221  
1222  
1223  
1224  
1225  
1226  
1227  
1228  
1229

**Figure 4** Time-Latitude cross section of precipitation during the event averaged over East China (denoted as the black box in Fig. 2) from the CMA station observations and the simulations with the global uniform and variable resolutions with two convective parameterizations. The modeling results are sampled at the CMA stations.

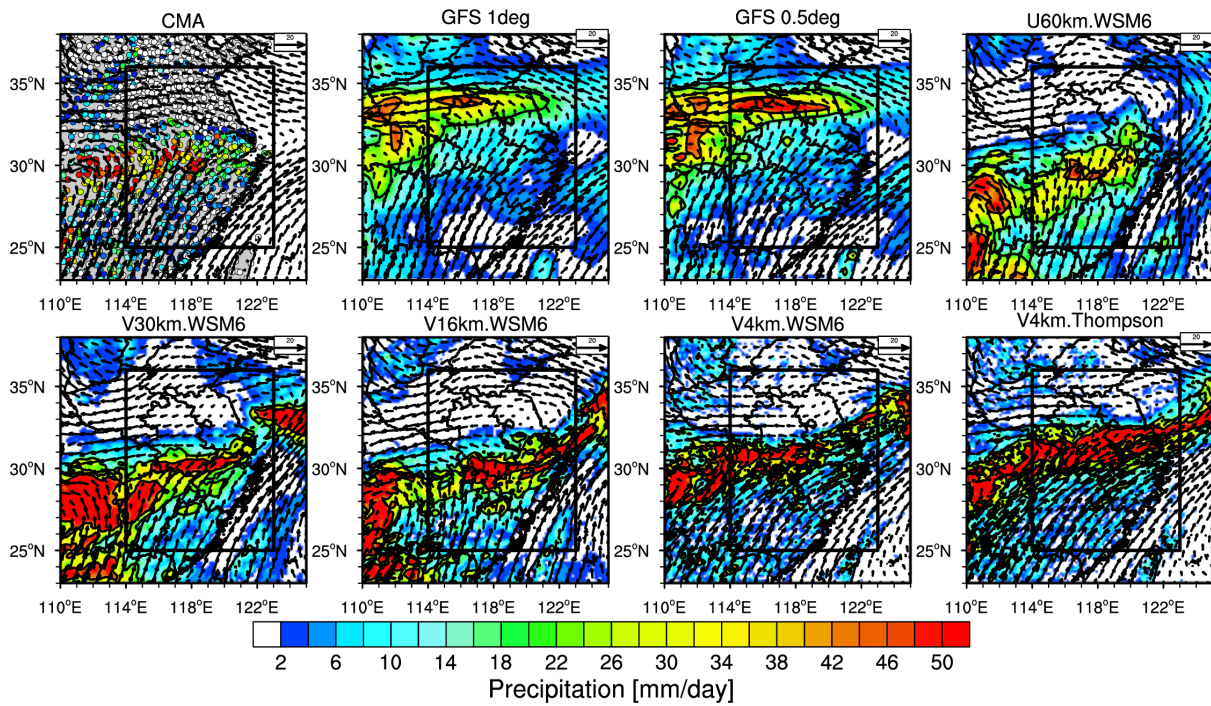
1230  
1231  
1232  
1233  
1234  
1235



1236  
1237  
1238  
1239  
1240  
1241  
1242  
1243  
1244  
1245  
1246  
1247  
1248  
1249  
1250

**Figure 5** Spatial distribution of averaged parameterized and resolved precipitation during the event over East China from the simulations with the resolutions of 60 km, 16 km, and 4 km.

1251  
1252  
1253  
1254  
1255  
1256

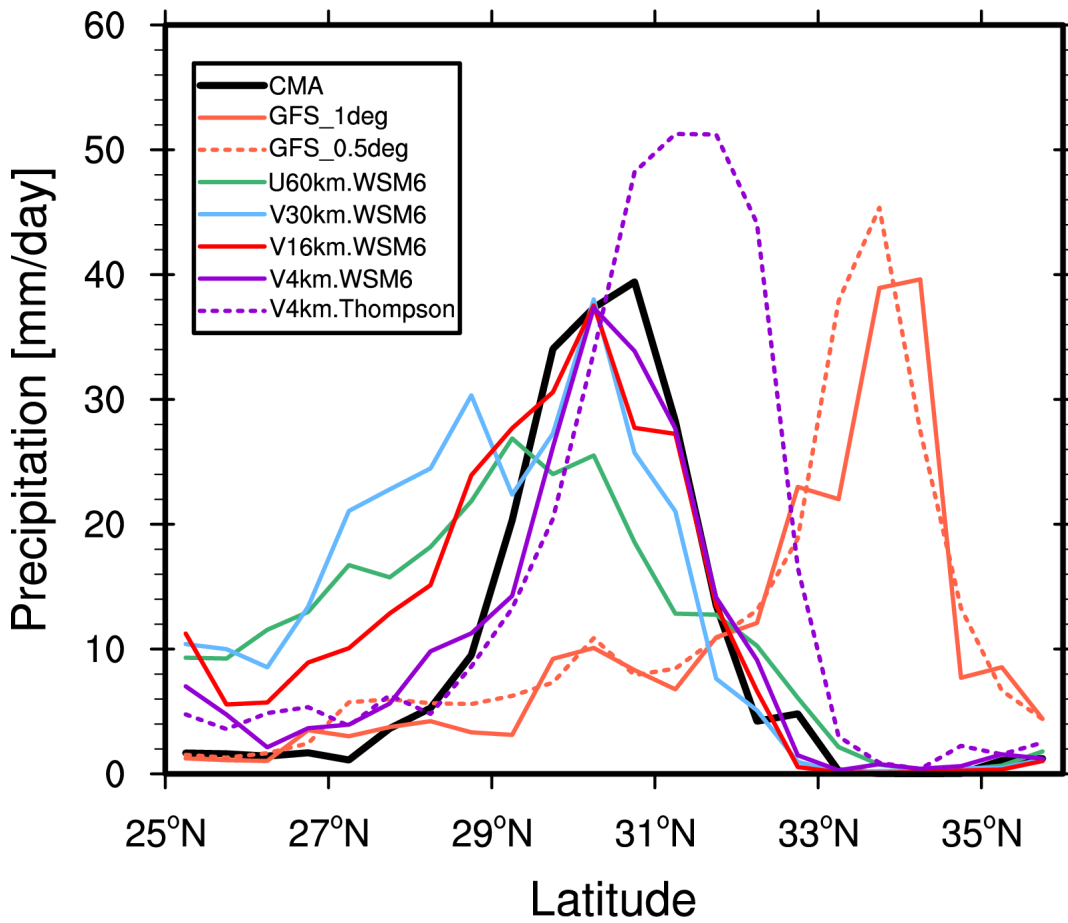


1257  
1258  
1259  
1260  
1261  
1262  
1263  
1264  
1265  
1266  
1267  
1268  
1269  
1270  
1271  
1272

**Figure 6** Spatial distributions of precipitation and wind fields at 850 hPa averaged during the event from the MPAS simulations at the resolutions of 60 km, 30 km, 16 km, and 4 km. The observed mean precipitation from the CMA stations and the wind fields from the ERA5 reanalysis are shown as well. The black contour lines represent the precipitation larger than 20 mm/day. The black box denotes the region of East China (25°N-36°N, 114°E-123°E) for the analysis in the following. For comparison, the GFS forecasts at 1 degree and 0.5 degree resolutions are also shown.

1273

1274



1275

1276

1277 **Figure 7** Zonal distributions of precipitation averaged during the event averaged over East  
1278 China (denoted as the black box in Fig. 6) from the CMA station observations and the  
1279 simulations with the resolutions of 60 km, 30 km, 16 km, and 4 km. For comparison, the GFS  
1280 forecasts at 1 degree and 0.5 degree resolutions are also included. The modeling results are  
1281 sampled at the CMA stations.

1282

1283

1284

1285

1286

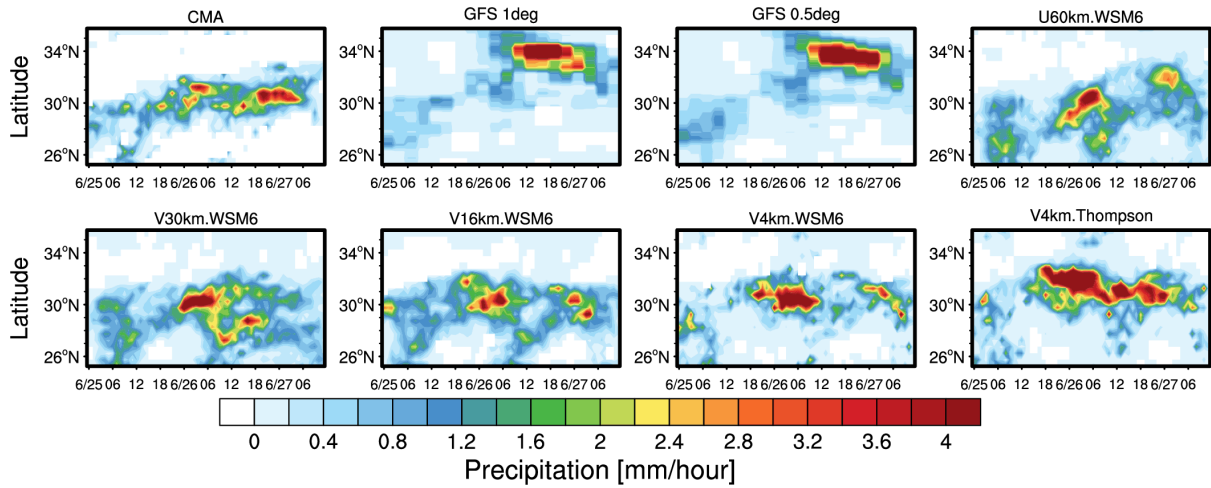
1287

1288

1289

1290

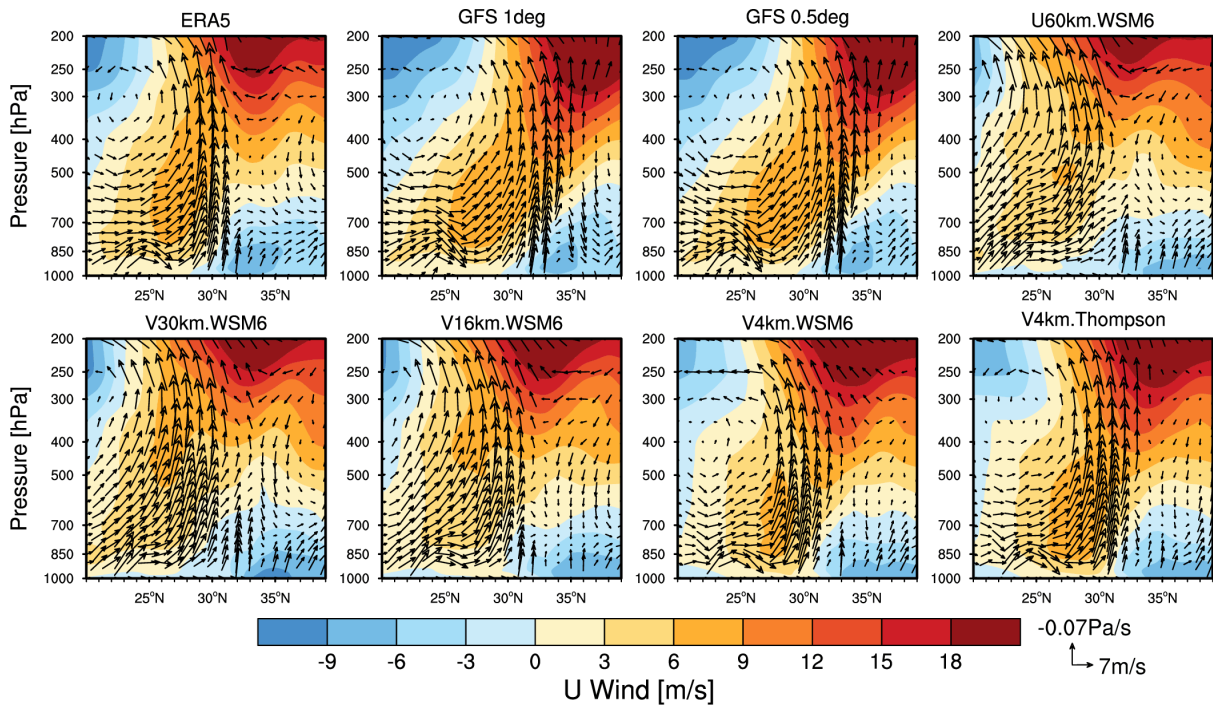
1291  
1292  
1293  
1294



1295  
1296  
1297  
1298  
1299  
1300  
1301  
1302  
1303  
1304  
1305  
1306  
1307  
1308  
1309  
1310  
1311  
1312  
1313  
1314  
1315

**Figure 8** Time-Latitude cross section of precipitation during the event averaged over East China (denoted as the black box in Fig. 6) from the CMA station observations, GFS forecasts at 0.5° and 1.0° resolutions, and the MPAS simulations at resolutions of 60 km, 30 km, 16 km, and 4 km over East China. The simulations at 4 km are with two cloud microphysics schemes (WSM6 and Thompson). The modeling results are sampled at the CMA stations.

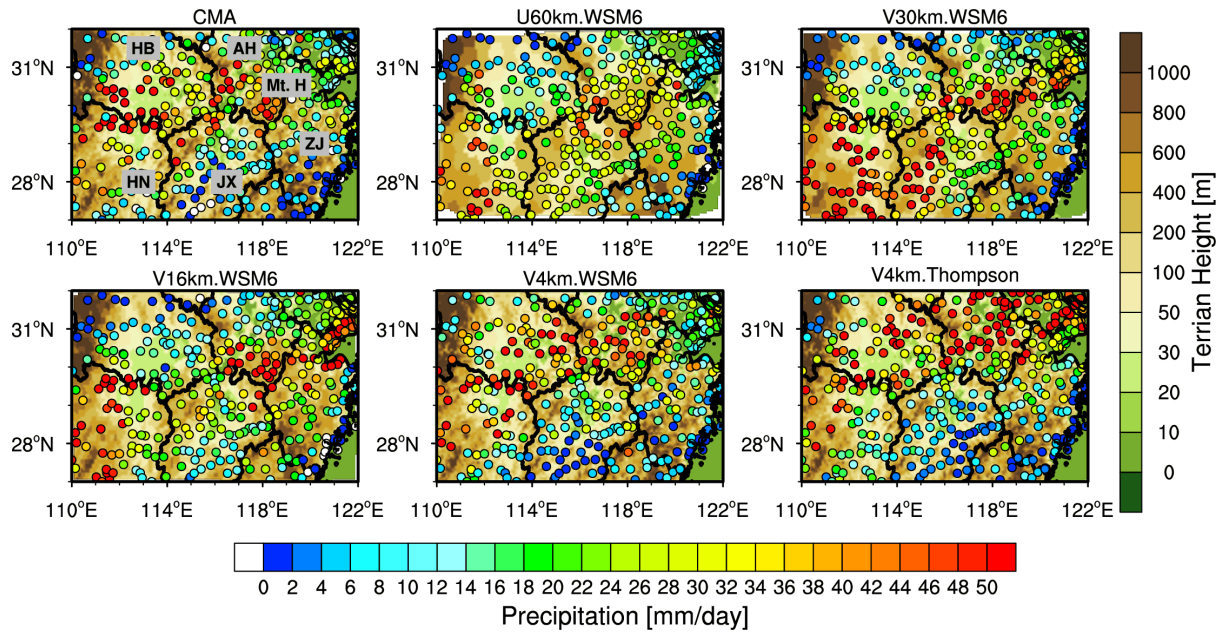
1316  
1317  
1318  
1319  
1320  
1321



1322  
1323  
1324  
1325  
1326  
1327  
1328  
1329  
1330  
1331  
1332  
1333  
1334  
1335  
1336

**Figure 9** Height-Latitude cross section of wind fields averaged over the region (the entire domain as shown in Fig. 6) during the event from the ERA-interim reanalysis, the GFS forecasts at 0.5° and 1.0° resolutions, and the MPAS simulations at resolutions of 60 km, 30 km, 16 km, and 4 km. The simulations at 4 km are with two cloud microphysics schemes (WSM6 and Thompson). The positive color represents eastward wind. All the datasets are regridded into 0.25° horizontal resolution.

1337  
1338  
1339

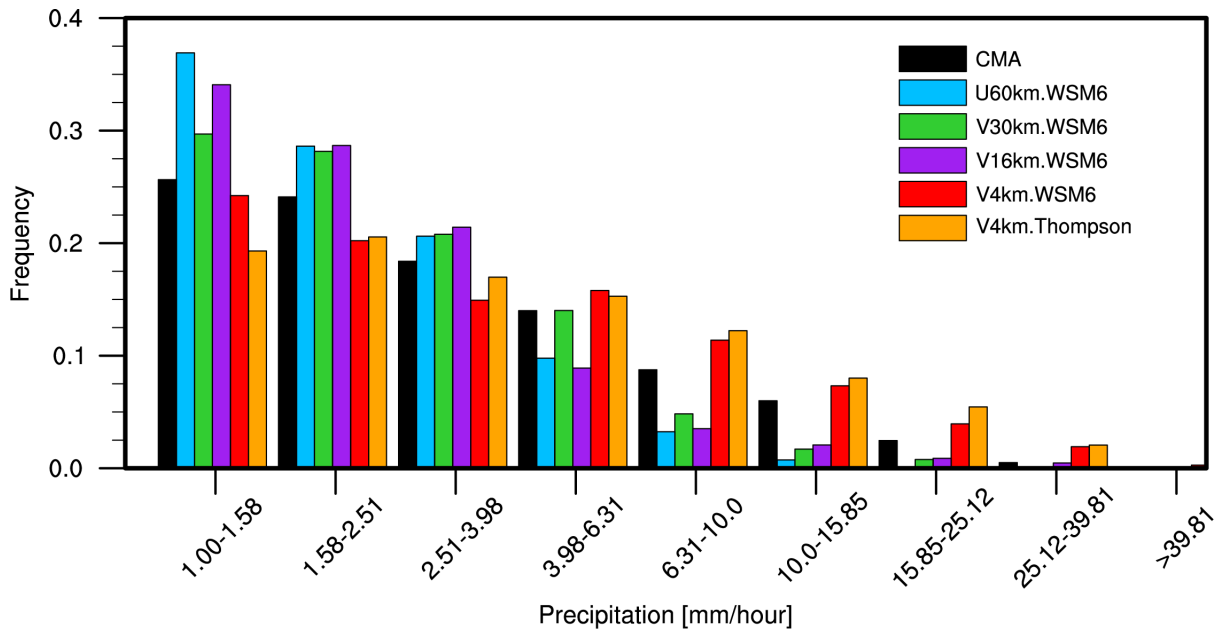


1340  
1341  
1342  
1343  
1344  
1345  
1346  
1347  
1348  
1349  
1350  
1351  
1352  
1353  
1354  
1355  
1356  
1357  
1358  
1359

**Figure 10** Spatial distributions of precipitation averaged during the event over the heavy precipitation region (27°N-32°N and 110°E-122°E) from the CMA observations and the MPAS simulations at the resolutions of 60 km, 30 km, 16 km, and 4 km. The simulations are sampled at the CMA stations. The topography is also shown. In the panel of CMA result, “AH”, “ZJ”, “HB”, “HN”, “JX”, and “Mt. H” denote the provinces of Anhui, Zhejiang, Hubei, Hunan, and Jiangxi, and Mountain Huang, respectively.

1360

1361



1362

1363 **Figure 11** Probability density functions (PDFs) of hourly precipitation at all the CMA stations  
1364 during the event over East China (denoted as the black box in Fig. 6) from the CMA  
1365 observations and the MPAS simulations at the resolutions of 60 km, 30 km, 16 km, and 4 km.  
1366 The simulations are sampled at the CMA stations.

1367

1368

1369

1370

1371

1372

1373

1374

1375

1376

1377

1378

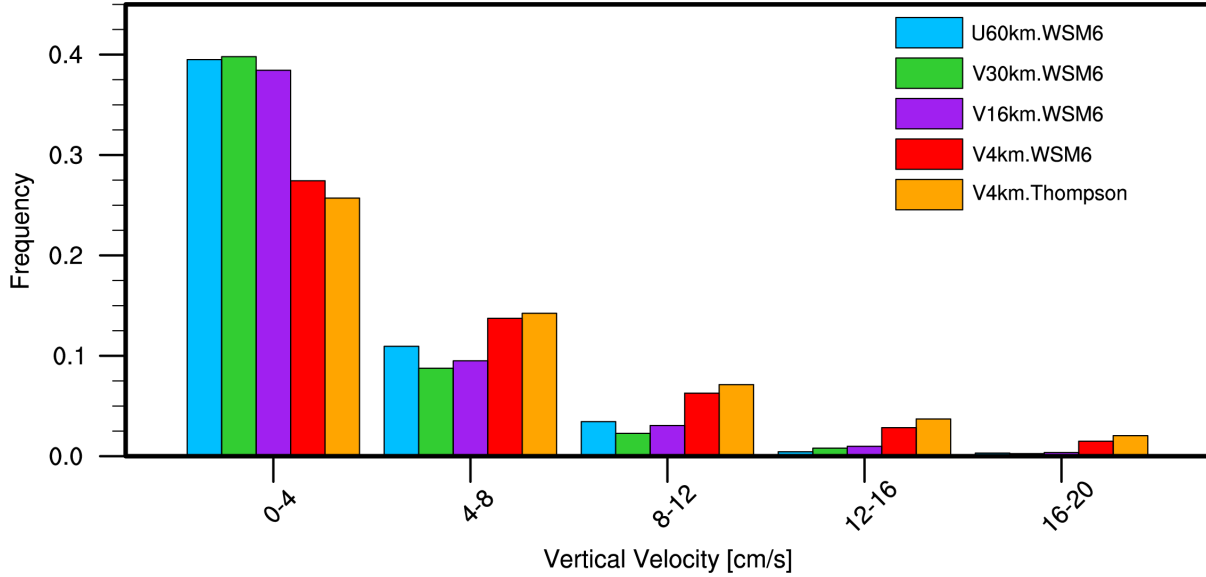
1379

1380

1381

1382

1383  
1384  
1385  
1386

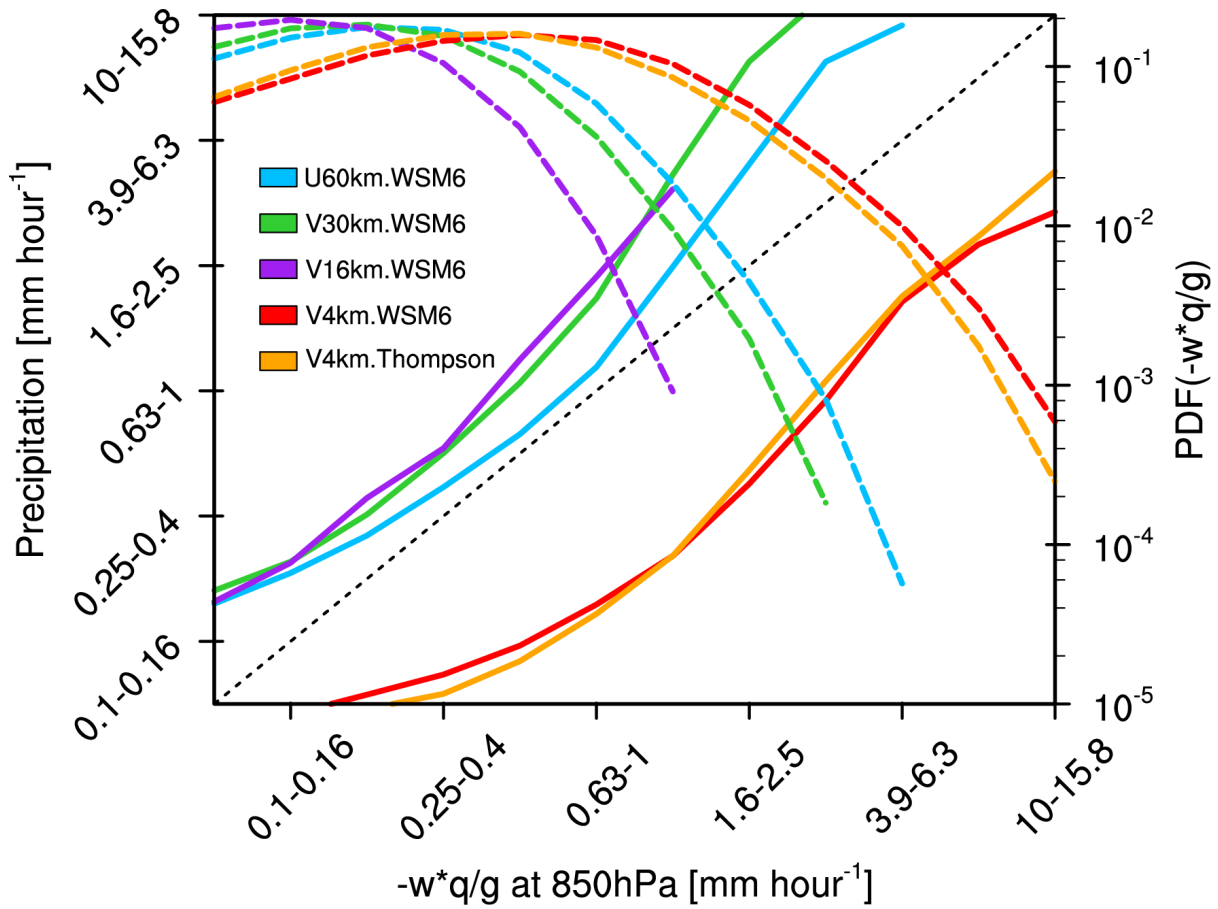


1387  
1388  
1389  
1390  
1391  
1392  
1393  
1394  
1395  
1396  
1397  
1398  
1399  
1400  
1401  
1402  
1403  
1404  
1405  
1406

**Figure 12** Probability density functions (PDFs) of hourly upward vertical velocity averaged below 700 hPa at all the CMA stations during the event over East China (denoted as the black box in Fig. 6) from the MPAS simulations at the resolutions of 60 km, 30 km, 16 km, and 4 km.

1407

1408



1409

1410 **Figure 13** Hourly precipitation versus upward moisture flux at 850hPa during the event over  
1411 East China (denoted as the black box in Fig. 6) from the MPAS simulations at the resolution  
1412 of 60km, 30km, 16km and 4km (solid line, left axis), and the PDFs of the upward moisture  
1413 flux (dash line, right axis).

1414

1415

1416